

Dynamically Tunable Localized Surface Plasmons using VO₂ Phase Transition

by

EESA RAHIMI

Submitted to the Graduate School of Sabanci University
in partial fulfillment of the requirements for the degree of
Doctor of Philosophy

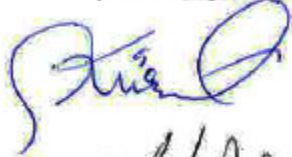
Sabanci University

July 2017

**DYNAMICALLY TUNABLE LOCALIZED SURFACE
PLASMONS USING VO2 PHASE TRANSITION**

APPROVED BY:

Prof. Dr. Kürşat Şendur
(Thesis Supervisor)



Assoc. Prof. Dr. Ahmet Onat



Assoc. Prof. Dr. Burç Mısırlıoğlu



Assoc. Prof. Dr. Hakan Ertürk



Assoc. Prof. Dr. Erdem Öğüt



DATE OF APPROVAL: 27/07/2017

© Eesa Eahimi 2017

All Right Reserved

ABSTRACT

DYNAMICALLY TUNABLE LOCALIZED SURFACE PLASMONS USING VO₂ PHASE TRANSITION

EESA RAHIMI

Mechtronics Engineering, Ph.D. Thesis, 2017

Thesis Supervisor: Prof. Dr. Kürşat Şendur

Keywords: Localized surface plasmons, VO₂ phase transition, Femtosecond pulse shaping, Yagi-Uda antenna, Chimera states

The control of light with plasmonic devices in practical applications require dynamic tunability of localized surface plasmons. Employing phase change materials in plasmonic structure enables it to respond to light dynamically depending the external stimulate. This study investigates the response in presence of vanadium dioxide (VO₂) phase transition for numbers of novel and classic problems.

To illustrate the significance of optical spectrum tunability by VO₂ two important functionalities for the phenomenon have been introduced. In the first application, a compact and ultrathin plasmonic metasurface is suggested for an ultra-short pulse shaping of transmitted pulse based on linear filtering principle of electromagnetic wave. It is demonstrated that the tunable optical filter by VO₂ phase transition can compensate real-time input carrier frequency shifts and pulse span variations to stabilize the output pulse. Second application is dedicated to the field of intrachip optical communication which shows how VO₂ phase transition can effectively switch a communicating antenna on and off. A substantial directional gain switching is obtained by employing VO₂ phase transition

to alternate resonances of a Yagi-Uda antenna elements. VO₂ scattering functionality in absence of localized surface plasmons is studied to illustrate their promising performance in light reflection. Finally the behavior of localized surface plasmon resonators is studied and chimera states which are the concurrent combination of synchronous and incoherent oscillations in a set of identical oscillators is shown for the first time in the optical regime. The effect of coupling strength on the phase space/synchronization of the spaser-based devised oscillators is investigated.

ÖZET

VO₂ FAZ GEÇİŞİ KULLANARAK DİNAMİK OLARAK AYARLANABİLİR YEREL YÜZEY PLAZMONLARI

EESA RAHIMI

Mekatronik Mühendislik Programı, Doktora Tezi, 2017

Tez Danışmanı: Prof. Dr. Kürşat Şendur

Anahtar Kelimeler: Lokalize yüzey plazmonları, VO₂ faz geçişi, Femto saniye darbe şekillendirme, Yagi-Uda anteni, Chimera evreleri

Pratik plazmonik uygulamalardaki cihazlarla ışığın kontrolü, lokalize yüzey plazmonlarının dinamik olarak ayarlanabilmesini gerektirir. Plasmonik yapıda faz değişim materyali kullanmak, dış uyarana bağlı olarak ışığa dinamik olarak yanıt vermesini sağlar. Bu çalışma, vanadyum dioksit (VO₂) faz geçişinin varlığında, yeni ve klasik problemlerin cevaplarını araştırmaktadır.

VO₂ ile optik spektrum ayarlanabilirliğinin önemini göstermek için, fenomenin iki önemli işlevselliği tanıtıldı. İlk uygulamada, elektromanyetik dalganın doğrusal filtreleme prensibine dayanan nakledilen nabzın aşırı kısa darbe şekillendirilmesi için kompakt ve ultra ince bir plasmonik meta yüzey önerilmektedir. Ayarlanabilir optik filtrenin, çıkış nabzını stabilize etmek için gerçek zamanlı giriş taşıyıcı frekans kaymalarını ve darbeleri yayılımlarını telafi edebildiği gösterilmiştir. İkinci uygulama, VO₂ faz geçişinin iletişim kuran bir anteni etkin bir şekilde açıp kapatabildiğini gösteren, cihaz içi optik iletişim alanına ayrılmıştır. Yagi-Uda anten elemanlarının alternatif rezonanslarına VO₂ faz geçişini kullanarak önemli bir yönlü kazanç geçişi elde edilir. Lokalize yüzey plazmonlarının yokluğunda VO₂ saçılma işlevselliği, ışık yansımadaki umut veren performanslarını göstermek için incelenmiştir. Son olarak, lokalize yüzey plazmon

rezonatörlerinin davranışı incelenmekte ve bir özdeş osilatör setinde senkron ve tutarsız salınımların eşzamanlı kombinasyonu olan kimerik istatistikler optik rejimde ilk defa gösterilmektedir. Bağlayıcı kuvvetin, spazere dayanan geliştirilmiş osilatörlerin faz tarifi/senkronizasyonu üzerindeki etkisi araştırılmıştır.

Acknowledgments

First and foremost, I would like to thank my supervisor Dr. Kürşat Şendur for giving the opportunity to carry out this research. I am deeply grateful for his support and invaluable expertise he has shared with me during my PhD years. Also I would like to thank the Scientific and Technological Research Council of Turkey (TUBITAK) for supporting my PhD under projects 113F171 and 115M033.

I wish to express my gratitude to my wife Yalda and to all my family members who always have been there for me. Their love and support have meant a lot to me during these 4 years.

TABLE OF CONTENTS

1	Introduction	1
1.1	Background and Motivation	1
1.2	Aim and Objective	4
1.3	Main Contributions	4
1.4	Thesis Outline	6
2	Ultrafast Pulse Shaping by Localized Surface Plasmons	8
2.1	Introduction	8
2.2	Temporal Control of Ultrafast Pulses using Metasurfaces	12
2.3	Metasurface Design for Femtosecond Pulse Control	16
2.4	Polarization Control of Femtosecond Pulses	20
2.5	Reconfigurable Metasurface	22
2.6	Dynamic Pulse Shaping	28
2.7	Conclusion	32
3	Switchable Plasmonic Yagi-Uda Antenna	34
3.1	Introduction	34
3.2	Isolated Radiator	36
3.3	Isolated Scatterer	38
3.4	Yagi-Uda Radiator	40
3.5	Discussion	43
3.6	Conclusion	44

4	Reflection Switching by VO2 Phase Transition in Core-Shells	46
4.1	Introduction	46
4.2	Reflectivity of VO2 Nano-sphere	47
4.3	Reflectivity of VO2@Si Core-shells	50
4.4	Conclusion	53
5	Chimera States in Optical Nano-resonators	54
5.1	Introduction	54
5.2	Oscillator Design	55
5.3	Chimera States Demonstration	59
5.4	Method	61
5.5	Conclusion	63
6	Conclusion and Future Works	66
6.1	Conclusions	66
6.2	Suggestions for Future Works	68

LIST OF FIGURES

1.1	Incident light interaction with metal's conduction electrons in plasmonic nano-particles [1]	2
2.1	Pulse shaping schematic using nano-plasmonic filter	9
2.2	Obtaining the transmission spectrum response of the periodic golden metasurface on a fused silica substrate with a 2 nm titanium adhesion layer: (a) the unit cell, (b) transmission magnitude and (c) transmission phase for $L_x = L_y = 200$ nm, $L = 100$ nm and $w = t = 20$ nm. h_{ab} indicates the transmission with a-polarized input and b-polarized output. The cross-polarization is zero which is not plotted.	13
2.3	Pulse shaping with a golden monobar array, $L = 150$ nm, $w = 50$ nm, $t = 30$ nm, $L_x = 200$ nm, $L_y = 100$ nm, 2 nm titanium adhesion layer on a fused silica substrate. (a) transmission spectral response, (b) input/output comparison for different pulse width at $f_c = 370$ THz, (c) input/output comparison for $\Delta t = 7.5fs$ but different f_c , (d) and (e) compression rate for (b) and (c)	16
2.4	Half power pulse width compression of a Gaussian pulse with $f_c = 370$ THz by different metasurface filters. In all cases: $L_x = 200$ nm, $L_y = 100$ nm the golden monobar array has $t = 20$ nm and is adhered to the fused silica substrate with a 2 nm titanium adhesion.	17

2.5	Filter design based on input and output spectrum. Gaussian input (blue)/output (red) spectrum in pulse expansion case (a) and in pulse compression case (b). The important frequency range of the input is specified by a double arrow in each subfigure. The filter spectral response (blue) and the normalized filtered output spectrum (red) for pulse expansion (c) and pulse compression (d).	18
2.6	(a) and (b) realized filters spectral amplitude (blue) and phase (red) response for the designed responses of Fig. 2.5. (c) and (d); comparison of the normalized input and output pulses, (c) pulse expansion case and (d) pulse compression case.	21
2.7	Linear to circular polarization conversion of the ultrafast pulse by the metasurface. (a) the metasurface and tilted linear-polarized input, (b) magnitude and (c) phase of the transmission for a golden monobar array with $L = 100$ nm, $w = 30$ nm, $t = 30$ nm, $L_x = 120$ nm, $L_y = 100$ nm and a 2 nm titanium adhesion layer on fused silica. (d), (e) and (f) the polarization shaped pulsed Gaussian pulse of durations 10fs, 20fs and 30fs	22
2.8	(a) Dynamic pulse shaping schematic by reconfigurable localized surface plasmon based on insulator to metal phase transition of VO ₂ . (b) real and (c) imaginary parts of VO ₂ relative permittivity changes by temperature. The darkest red shows the material property at 73 °C and brighter reds represent the property at higher temperatures up to 85 °C	23
2.9	Transmission coefficient's amplitude (a) and phase (b) of a metasurface devised for thermal controlling of band-stop optical filter's dip strength in several temperatures. Transmission coefficient's amplitude (c) and phase (d) for a metasurface with thermally controlled stop frequency filtering in different temperatures.	26

2.10	Half-power pulse span compression (red) and expansion (blue) percentage for various pulses with variable carrier frequencies and spans at different temperatures	28
2.11	(a) The transmission coefficient phase slope represented in the form of a narrow-band pulse delay versus temperature at 150 THz for optical filter of Fig. 2.9 (a and b). (b) Maximum amplitude variation of the transmission coefficient in 150 THz $\pm(5\%)$ range.	30
2.12	(a) Multilayer parallel metasurfaces with independent thermal controls which oblique incident angle and appropriate distance between the metasurfaces avoid multi-reflections to the output. Pulse shape preservation for variable carrier frequency (b) and variable pulse span (c) using the configuration shown in (a).	31
3.1	Normalized spectral radiation power (integrated over all 4π steradians for each frequency) of a QD fed single radiator at $30^{\circ}C/85^{\circ}C$. The radiator antenna consists of a gold cavity cylinder of length 275 nm and diameter of 100 nm which is covered with 70 nm of VO ₂ coating. The voltage across VO ₂ causes heating by current flow and adjusts temperature. Antenna radiation pattern is shown in linear scale at resonance i.e. $\lambda = 1500$ nm, $T = 30^{\circ}C$	36
3.2	Spectral comparison of induced current at the midpoint of the gold nanorod due to plane wave incidence for different rod lengths and temperatures. (a) normalized amplitude and (b) corresponding phase with reference to the incident electric field phase.	39
3.3	Induced current at designed Yagi-Uda elements due to QD excitation of feed element at low/high temperatures. (a) normalized amplitude and (b) phase difference of parasitic elements currents from driven feed currents.	41

3.4	A comparison between designed single radiator and Yagi-Uda radiation patterns at low/high temperatures. (a) single radiator (SR) antenna and its patterns shown in log scale, (b) Yagi-Uda radiator (YR) and its patterns drawn in log scale, (c) Normalized antennas patterns at azimuth in dB scale.	43
4.1	(a) Normalized back-scattering cross-section of insulator VO2 at $\lambda = 2000$ nm as a function of particle radius. (b) Power reflection by a 2-D array of VO2 spheres with $r = 320$ nm and lattice period of $a = 1000$ nm upon normal incident of light at mid-infrared wavelengths. Increasing ambient temperature from $T = 30$ °C to $T = 85$ °C changes the optical index of VO2, consequently, the reflectivity of the array switches. . . .	49
4.2	Power reflection by a 2-D array of VO2@Si core-shells with $r = 320$ nm and lattice period of $a = 1000$ nm upon normal incident of light at mid-infrared wavelengths for $T = 30$ °C to $T = 85$ °C and different Si thicknesses.	51
4.3	Power reflectivity by a 3-D array of randomly distributed VO2@Si core-shells at $T = 30$ °C and $T = 85$ °C. The nano-particles radius is 320 nm and Si has 30 % of the overall thickness.	52
5.1	Plasmonic nano-oscillator (a) Geometry and excitation illustration. (b) Electric field enhancement of the plasmonic dimer at the center of its gap before doping InP. (c) Time-profile of the electric field excitation. (d) Probed electric field at the dimer gap. (e) Electron population density normalized to the density of active molecules in InP at the center of the plasmonic dimer.	57
5.2	An example of full coherency in the oscillator array: (a) Geometry of the array, (b) Probed electric field at the center of oscillator 1, (c) The amplitude of oscillation for different oscillators over time.	64

5.3	Sampled phase of the oscillators electric field at their gap for different array geometries: (a) $r = 27.5$ nm, (b) $r = 35$ nm, (c) $r = 70$ nm and (d) $r = 140$ nm.	65
5.4	Simplified model of electron interaction with photons in an active medium with 2 electron 4 energy level atomic system.	65

Chapter 1

Introduction

1.1 Background and Motivation

Optical properties of metals and some of their compounds can be explained by plasma model over a broad frequency range, where a gas of free electrons moves against a fixed background of positive ion cores [2]. The electron oscillation of this gas in response to applied electromagnetic field has fascinating properties. It can confine electromagnetic fields over sub-wavelength dimensions and enhance it in the near-field region of metallic particles. These localized surface plasmons (LSP) are highly efficient at light absorption and scattering; they have paved the way for many nano-scale applications, such as photodetection [3,4], photovoltaic devices [5], higher harmonic generation [6], femtosecond pulse shaping [7], optical active devices [8], sensing [1] and so on.

Electric field enhancement and absorption/scattering properties of the particle depends on the resonance strength which is a function of geometry and the material's optical index. Once the geometry, material and surrounding environment of the particle are chosen, resonance frequency is fixed [9]. However, phase change materials (PMC) that have variable optical permittivities [10] can be incorporated in the LSP structure to alter the resonance frequency dynamically by an external stimuli. This method is the easiest way to change the LSP's optical response comparing to mechanical methods that modify the geometry by applying strain or stress [11], employing

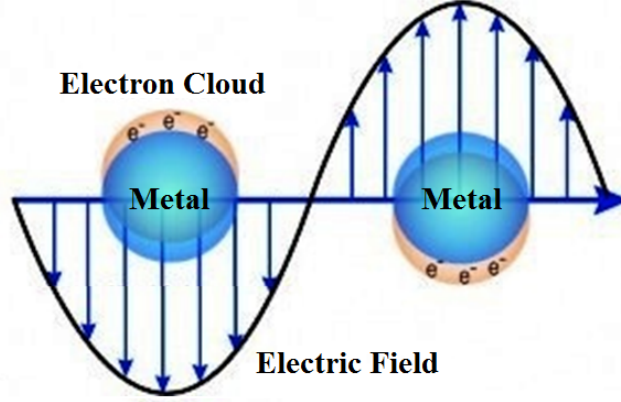


Figure 1.1: Incident light interaction with metal's conduction electrons in plasmonic nano-particles [1] elastic substrates [12] or heat [13].

Phase change materials have been extensively used in electronics for devising high performance transistors [14, 15] where hybrid-phase-transition is employed to steepen the switching performance of field-effect transistors by intrinsic metal to insulator transformation (MIT) of vanadium dioxide. Their ability to react to heat made them potential candidate for thermal rectifiers [16–18] and amplifiers [19]. However, the greater input of these materials in the field of nano-photonics where they are employed to manipulate light waves. They have been employed in thin film structures in order to control transmission and reflection from them [20, 21]. The tunable properties of them provided an exciting opportunity to modulate optical response of thin films [22, 23].

PCM's contribution on the controlling light scattering of nano-plasmonic particle is very fascinating. VO₂ bars can tailor magnetic resonance in metamaterial structure [24] and as a result tune the light absorption spectrum. PCM have been also used in other configurations that provide tunable absorbance by electromagnetic resonance of plasmonic particles [25]. It can be employed as a substrate to tune the resonance of plasmonic nano-particle arrays to control reflection from their surface [26]. There are many examples of meta-material's transmission/reflection (TR) manipulation by PCM [27–33] as a substrate in terahertz and optical regime. Particularly in split ring resonators showed considerable sensitivity to the substrate material phase transition [27, 29, 30]. Switching the polarization conversion and chirality is also achievable when

the PCM is employed as a particle substrate in a configuration like patch antennas [34] or when it is employed as an inter-particle spacer [35].

Due to sensitivity of LSPs to the permittivity of their hot-spots, voltage-dependent graphene sheets have been employed there to control their optical resonances [36]. Resonance based optical sensors on the other hand work based on this principal and their sensitivity increases as the permittivity change happens closer to their hot-spots [37]. Using phase change materials at these points have a greater impact in controlling their scattering properties [38, 39]. This trend can be employed for many applications with electromagnetic hotspots such as nano-plasmonic dimmers, polymers, holes, patches and scatterers. Specifically, nano-scale optical communication antennas can benefit from versatile plasmonic resonances to enable radiation control while the alternative methods such as metal/semiconductor non-linearity manipulation [40–43] are not power-efficient and affordable.

On the other hand, VO₂ phase transition in core-shell structures embedded inside a transparent host medium can manipulate transmitted light spectrum [44] and as a result boosts thermo-chromic materials and smart windows [45]. Nonetheless the ability of these particles to effectively manipulate reflection from objects has been missed in the literature. Existing works focus on transmission spectrum modification and rarely use PCM in conjunction with an insulator Mie scatterer [46]. Insulator Mie scatterers which have quite lower intrinsic loss rates compared to metals have been used as frequency selective paint pigment because of their highly reflective properties at visible range of light. In these nano-particles size tuning modifies the resonance and as a result the reflection rate changes [47–49]. There is no control over the reflectivity after tuning the particle size. Adding VO₂ to the scatterers can transform them to a switchable reflector but the material appliance has to be devised to avoid high loss rates of VO₂ at its insulator reflective state, enjoying this loss at the metallic absorptive format.

1.2 Aim and Objective

The main aim of this dissertation is to study the effect of VO₂ phase transition the LSP resonance and investigate how this material can be effectively employed in different applications which require dynamic tunability. Then the following objectives are pursued in this research:

- Utilizing localized surface plasmon resonances to manipulate light spectrum and employing this idea for ultrashort pulse duration and polarization shaping applications.
- Dynamic tuning/switching of the LSP resonances by VO₂ phase transition and how this material can effectively applied to an optical meta-materials for pulse shaping application.
- Investigating the effect of resonance shift by VO₂ phase transition on the radiation efficiency of nano-plasmonic antennas. Study their implementation in a Yagi-Uda antenna for inter/intra-ship optical communication systems.
- Employing VO₂ phase transition for the reflectivity control from nano-particle arrays and enhancing the frequency-dependent reflection coefficient controllability from these structures using insulator@VO₂ core-shells.

Investigation of optical nano-oscillator using LSP resonators and the synchronization behavior of identical oscillators in arrays are interesting topics which have been studied during this PhD. Therefore, demonstrating concurrent combination of synchronous and incoherent oscillations in a set of identical oscillators is added to the objective of this thesis.

1.3 Main Contributions

This dissertation contributes to the field of nano-plasmonics. Specifically, it introduces novel techniques to the field of ultra-short pulse shaping, nano-optical signal processing,

integrated nano-optics, solar energy harvesting and non-linear systems. The primary objective of this dissertation is to investigate the dynamic tunability of localized surface plasmons using VO₂ phase transition for emerging applications and technologies in optical regime.

The research develops a novel and versatile technique for processing ultrashort optical pulses which competes with the existing methods and technologies due to its simplicity and compact size. That makes the integration of essential ultrashort pulse shaper happen in nano-optics and in the new generation of ultra compact optical processors. Based on the outcomes of this research a journal paper is published and one more is under review for publication in high impact journals. The published work received a considerable attention in a short period of time and was cited 3 times in journals such as Physical Review Applied and APL Photonics.

This dissertation adds to field of on-chip optical communication by introducing a switchable directive nano-plasmonic antenna. Due to high losses of plasmonic waveguide, antenna-to-antenna connection will take the lead in on-chip optical communication. Therefore this portion of the research plays an important role in technology development specifically because of its dynamic tunability and realistic implementation. A paper is published in a high ranked journal in the field of optical communication based on the outputs of the dissertation.

This study investigates the chimera states in nano-optics for the first time in literature. The interesting effect plays an important role in analysis of nano-optical oscillator arrays behavior because of their application in periodic structure of optical meta-materials. This dissertation also contributes to the development of non-linear oscillator and high quality factor plasmonic resonators. A paper is submitted to a very prestigious journal in physics based on the achievements of this dissertation.

The dissertation also has minor but important contribution to the field of solar energy harvesting by introducing a reflectivity switchable coating. A manuscript is under preparation for publication in a very good journal of spectroscopy community.

The list of extracted scientific papers from the dissertation comes below. The pub-

lished works are:

- Eesa Rahimi and Kürşat Şendur, "Femtosecond pulse shaping by ultrathin plasmonic metasurfaces." *JOSA B* 33.2 (2016): A1-A7.
- Eesa Rahimi and Kürşat Şendur, "Temperature-driven switchable-beam Yagi-Uda antenna using VO₂ semiconductor-metal phase transitions." *Optics Communications* 392 (2017): 109-113.

The submitted manuscripts to the scientific journals are:

- Eesa Rahimi and Kürşat Şendur, "Thermally controlled femtosecond pulse shaping using metasurface-based optical filters." under review in *Journal of Optics*.
- Eesa Rahimi and Kürşat Şendur, "Chimera states in nano-optical resonators" submitted for publication in *Physical Review Letters*.

The under preparation work is:

- Eesa Rahimi, Burç Mısırlıoğlu, Serkan Ünal, Yusuf Menciloğlu and Kürşat Şendur, "Switching core-shell nanoparticles reflective spectrum using vanadium dioxide phase transition" prepared for submission to the *Journal of Quantitative Spectroscopy & Radiative Transfer*.

1.4 Thesis Outline

The thesis is divided to 4 main chapters each include their own review, methodology and results, followed by a conclusion chapter which summarizes the research and make suggestion to further expand this study. Each main chapter pursues one or two of the defined objectives in the aim and objective list.

Chapter 2 studies light spectrum transmission through arrays of localized surface plasmons and shows that how these optical filters affect the temporal profile of ultra-short pulses. Then VO₂ phase transition is employed to dynamically control the pulse shaping by temperature tuning in mono-layer or multi-layer metasurfaces. Chapter

3 investigates the effect of VO₂ phase transition on the switchability of nano-optical communication antenna. The radiation pattern of the antenna under different temperatures is studied and the effect of VO₂ losses at its metallic phase on the antenna is investigated.

In chapter 4, reflection switchability by VO₂ phase transition in objects with comparable size to the optical wavelength will be studied. It will be shown that how the core-shells of Si@VO₂ may enhance the reflectivity of the structure in arrays and random distributions in composites. Chapter 5 is dedicated to study of nano-optical oscillators. First an optical nano-oscillator is devised based on LSP resonance and then their synchronization behavior is investigated. Chapter 6 summarizes and concludes the work by suggesting potential future works to extend the research.

Chapter 2

Ultrafast Pulse Shaping by Localized Surface Plasmons

2.1 Introduction

During recent decades, optical pulses with a very short duration of several femtoseconds found in many applications in science and technology ranging from coherent control of chemical reactions [50–52] to lightwave and radio frequency communications [53–55]. While lasers provide a reliable source of short optical waves, the shaping of their temporal profile is still a challenge. Not only the shaping of the source pulses, but also the compensation of pulse deformation in transmission lines and power amplifiers is necessary for most applications. Widely used pulse shapers generally employ spatial filtering [55] which requires bulky dispersers and huge masks that are integrated in a complex and precise manner [56]. They can provide accurate dynamic control over the pulse shape and polarization using programmable spatial light modulators as the mask. However, due to their complexity, bulkiness, alignment difficulty, and susceptibility to vibrations, their application is limited [56, 57]. Bragg grating in optical fibers which filters the optical pulse by frequency dependent reflections is another method of shaping ultra short pulses [57–60]. These grating based pulse shapers also have their own drawbacks such as narrow spectral line-width [57, 61]. Another approach for pulse-

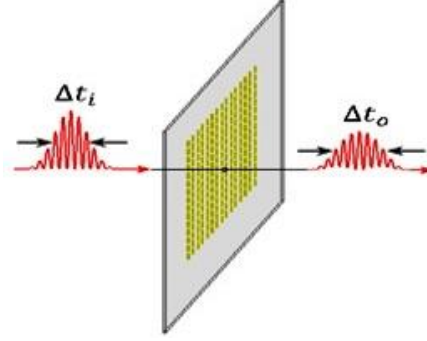


Figure 2.1: Pulse shaping schematic using nano-plasmonic filter

shaping is based on light-matter interaction as the pulse propagates. Nonlinear pulse shaping in optical fibers [62] and in bulk materials [63] are examples of this method.

An alternative approach for ultra short pulse shaping is based on the interaction of light with resonant nano-particles, which provides more compact solutions. Among these solutions, various groups have achieved spatio-temporal control of short pulses in the near-field zone of the particles [64–68]. Due to the interaction of particles with the input pulse, the temporal profile of electric field is altered by dispersion properties of the particle(s) [69,70]. The shape, phase, and polarization setting of the input pulse are important in concentrating the electric field in the specific region of the particles [66,71], which provide challenges for achieving the desired spatio-temporal control of short pulses. Particularly when the pulse is in the sub-100 femtosecond regime, the particles show narrow-band resonance characteristics compared to the input pulse’s spectrum. As a result, the output spectrum just broadens around these particles with limited control over its temporal profile. It should also be noted that a near-field shaped pulse might not necessarily be transformed into a propagating wave, which is essential for a number of ultra short pulse shaping applications.

Temporal control of short pulses can also be obtained by tailoring the reflection properties of metal film and plasmonic crystals [72–75]. Surface plasmon polaritons (SPP), which have comparable lifetimes to the excitation pulse in femtosecond regime, can modify the pulse shape during the scattering process. This scattering is highly sensitive to the carrier frequency of the metal film and plasmonic crystals. Its spectral

position compared to plasmonic Fano-type resonance [73] and polarization of excitation can be employed to control the polarization of the ultrashort pulse [75]. Despite the efficiency of the pulse-shaper, the output pulse includes a mixture of the ordinary and shaped reflections. Also, the complexity in the broadband excitation of the SPPs [76] makes the shaping of ultra short pulses inherently difficult. To make such a pulse-shaper robust and versatile, further research on the spectral properties of plasmonic crystals and their correlation to pulse shaping is desirable.

It has been widely reported in the literature that SPPs can shape the propagating optical spectrum through engineered resonances of nano-particles and lattice arrangements. Using this property, nonlinear propagation modes in a metal-dielectric interface can modify pulse duration and decay its intensity [77]. Although subwavelength metallic slits [69, 78] and holes [79–81] on plasmonic metals which show extraordinary transmission enhancement suffer from limited bandwidth, they are very good frequency bandpass linear filters [82, 83]. These band-stop filters have been employed to obtain negative refractive metamaterials by various groups [84–86]. Their scattering spectral response is widely studied for plasmon enhanced photovoltaic solar cells [87, 88]. Furthermore, nano-particles are employed in order to alter the polarization of the waves [89, 90], but not necessarily for polarization control of the pulsed waves. Even though the scattering properties of silver particles and clusters are studied to obtain their associated homogeneous dephasing time [91], their potential ability for shaping pulses has not been achieved. Transmission through the nano-plasmonic filters accompanied by absorption resonances of particles diminishes the spectrum transmission at certain frequency bands [92]. Therefore, temporal control of pulse-shape and polarization of ultra-short pulses can be achieved through engineered resonances of plasmonic nano-particles.

On the other hand, vanadium dioxide is shown to dynamically tailor optical phenomena through an impact on the refractive index of the physical systems upon an external stimuli such as temperature [93], intense light [94] or charge flow [95]. It undergoes a saturating but reversible insulator to metal phase transition in picosecond

time-scale [96] by heating from room temperature up to 85°C [10, 93, 97–99]. This phase transition has been exploited for plasmonic applications through its effect on the resonance properties of localized surface plasmons [24, 28, 100, 101]. Specifically, the lossy nature of VO₂ at high temperature in contrast with the lower loss insulating properties of VO₂ at low temperature has been proposed for tailoring the performance of opto-plasmonic devices [32, 102–104]. Here the phase transition in VO₂ is nominated to manage reconfigurability of LSPs to further facilitate the proposed pulse shaper.

In this chapter, first we propose a compact and ultra-thin plasmonic metasurface made of nano-particles for ultra-short pulse-shaping and polarization control of ultra-short pulses. We demonstrate that the transmission spectrum of the metasurface can be engineered to shape ultra-short pulse’s temporal characteristics. The metasurface is able to broaden and compress the duration and reshape the polarization of ultrashort pulses with great control. Then VO₂ phase transition will be employed to dynamically control the pulse shaper characteristics in real time. The outline of this study is as follows: In Section 2.2, a metasurface made up of an array of nano-bars is studied to investigate the various aspects of pulse shaping. In Section 2.3, the method for designing the required spectral response is devised to alter the temporal profile of the pulses. After that the devised spectral responses are realized using metasurfaces and their performance is reported. The polarization control of ultra-short pulses using the metasurface is shown in Section 2.4. Then we propose IMT in VO₂ for controlling the band-stop spectral lineshape of transmission coefficient through LSP metasurfaces. A Joule heating mechanism is proposed to control the thermal phase transition of VO₂ in an array of LSPs and corresponding voltage-temperature equation is extracted in Section 2.5. In this section temperature control of the phase transition in VO₂ is shown to manage reconfigurability of LSP transmission by changing the strength of its dip in one of the proposed filters and by shifting its resonance frequency in the other one. Using numerical simulations, the ability of these plasmonic filters for shaping femtosecond scale optical pulses is studied. The effect of temperature variation on the transmitted Gaussian pulses is characterized using Fourier analysis. It is shown that

the filters can provide a variable pulse span compression/expansion ratios depending on how the input spectrum is located with respect to the spectral lineshape of the filter. It is also demonstrated that the filter is able to apply variable phase shift to narrow-band pulses. To provide further functionality to the optical filter, we propose stacked filters that improve the pulse expansion and phase shifting abilities using a multilayer structure in Section 2.6. The introduced pulse shaper is able to thermally manipulate the band-stop lineshape of the filter to provide a wider control over the transmitted output pulse profile. Concluding remarks appear in Section 2.7.

2.2 Temporal Control of Ultrafast Pulses using Metasurfaces

In this study, the temporal control of ultrashort pulses is achieved by engineering the transmission spectrum of a planar metasurface, through which the spectrum of the incident ultrashort pulse is altered. The constituents of the metasurface used in this study are selected as linear materials, therefore the metasurface acts as a linear system. As a result, the frequency spectrum of the input and output can be associated using the impulse response of the system. In other words, if $E_i(\omega)$ represents the spectrum of the input electric field ($\omega = 2\pi f$), and the metamaterial system has the impulse response of $h(\omega)$, then the output electric field $E_o(\omega)$ is obtained through $E_o(\omega) = h(\omega).E_i(\omega)$. The impulse response of the system is not always known, therefore, it has to be designed or characterized. The important challenge of metasurface design for femtosecond pulse shaping are addressed in Section 2.3.

It is well-known that planar periodic structures are powerful means for tailoring spectral responses [84–86, 105–107]. In this section, the transmission spectrum of planar periodic structures upon normal light incidence are investigated through a finite element method based full-wave simulation of Maxwell equations using the Ansys program. The Floquet-Bloch theory is employed to reduce the problem to the study of a single cell of the structure. It imposes periodicity of the fields at the related boundaries of the unit cell. To obtain the transmission spectral response of a metasurface, the frequency is

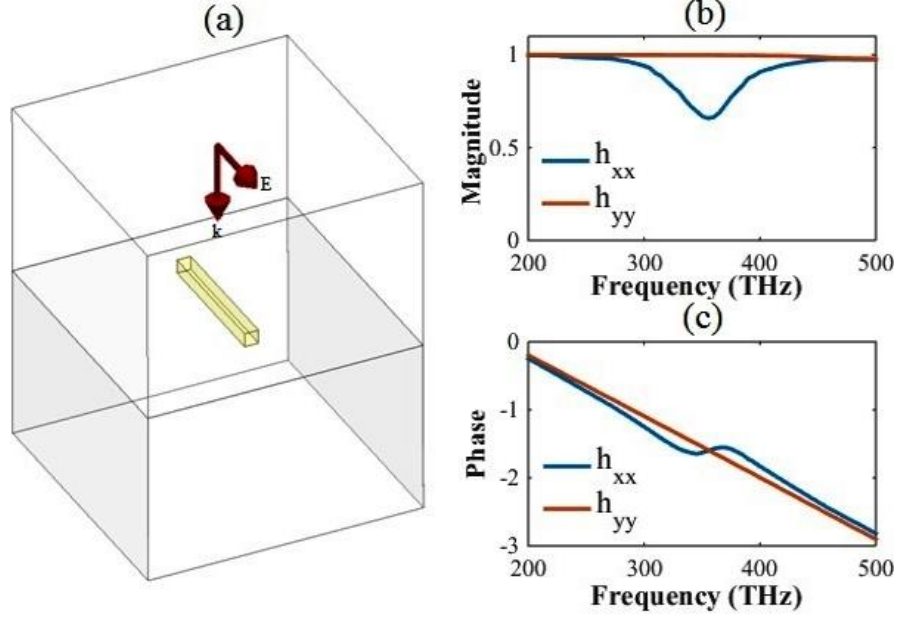


Figure 2.2: Obtaining the transmission spectrum response of the periodic golden metasurface on a fused silica substrate with a 2 nm titanium adhesion layer: (a) the unit cell, (b) transmission magnitude and (c) transmission phase for $L_x = L_y = 200$ nm, $L = 100$ nm and $w = t = 20$ nm. h_{ab} indicates the transmission with a-polarized input and b-polarized output. The cross-polarization is zero which is not plotted.

swept in different full-wave simulation executions. At each frequency, a plane wave is applied to the metasurface, then the amplitude and the phase of the transmission are recorded.

To investigate the spectral transmission characteristics of a typical metasurface used in this study, first periodic gold nano-particles deposited on fused silica are investigated. The lattice is periodic in the x-y plane with the periodicity of L_x and L_y . A bar-shaped nano-particle of length L (oriented in the x direction), width w and thickness t exists in each unit cell of the lattice. The nano-particle is placed onto a 500 nm thick fused silica with a 2 nm thick adhesion layer of titanium. In this study, the optical properties of gold and titanium nano-particles are extracted from the experimental work by Palik [108], fused silica's properties are extracted from Malitson's work [109].

Figure 2.2 illustrates the transmittance of the metasurface which is calculated for both a x and y-polarized input with $L_x = L_y = 200$ nm, $L = 100$ nm, $w = 20$ nm and $t = 20$ nm. In Fig. 2.2(a), a unit cell of the periodic metasurface is shown as a

reference. Fig. 2.2(b) and (c) represent the transmission of the structure for different polarizations. When the polarization is perpendicular to the antenna length, it passes through without any changes. However, when the input polarization is parallel to the antenna, a dip in the transmission spectrum is observed due to plasmon resonance. This dip in the transmission spectrum is due to the reflection and absorption of the input signal by the nano-particle array. The phase response line-shape also resembles the well-known second-order band-stop filter's phase. We emphasize the difference in transmittance for different polarizations, as this difference will be employed to control the output polarization in Section 2.4. The structure results in no polarization rotation.

After demonstrating a typical transmission spectrum for the metasurface, its ability to shape the temporal profile of pulses is examined. Obtaining the spectral response of the metasurface using the full-wave FEM solver, the output spectrum is obtained by multiplying the transmission response with the incidence pulse's spectral response. The temporal distribution of the output signal is obtained by taking an inverse Fourier transformation as:

$$E_o(t) = \frac{1}{2\pi} \int_{-\infty}^{+\infty} E_o(\omega) e^{-j\omega t} d\omega \quad (2.1)$$

In Fig. 2.3, temporal shaping of the output pulse through a metasurface is illustrated. First, the spectral transmission response of a golden monobar array with $L = 150$ nm, $w = 50$ nm, $t = 30$ nm, $L_x = 200$ nm, $L_y = 100$ nm and 2 nm titanium adhesion layer on fused silica is shown in Fig. 2.3(a). The structure resonates at 370 THz ($\lambda = 810$ nm). The metasurface alters the shape of the Gaussian-shaped input pulses depending on their characteristics. Fig. 2.3(b) shows how this filter transforms the Gaussian pulses with $f_c = 370$ THz but different half power pulse widths. As seen, the output pulses (red) are compressed compared to the input pulses (black). The percentage of compression of this experiment is shown in Fig. 2.3. (d). This figure indicates that the output can be compressed up to 22 % by the filter depending on the input half power pulse width Δt . Also, the ratio of the maximum of output intensity

to the maximum of input intensity is decreasing as pulse width increases. However, it is significant and so the power efficiency is quite comparable to the other linear and passive methods which alter spectrum amplitude [110]. Fig. 2.3(c) indicates how this filter transforms the Gaussian pulses with $\Delta t = 7.5$ fs but different central frequencies f_c . This figure illustrates that the output pulse (red) can either be compressed or expanded in comparison to the input (black). The frequency dependent compression of this experiment is shown in Fig. 2.3(e). The negative sign in the compression denotes that the pulse is expanded; as the figure shows expansion may reach 20% at input frequencies away from 370 THz. However, the ratio of the maximum of output intensity to the maximum of input intensity has a minima at the resonant frequency of the metasurface. Actually as the pulse's frequency becomes closer to the resonant frequency of the metasurface, more power is filtered by the metasurface and the output intensity decreases. In all cases the pulse shape has no side lobe and preserves its Gaussian shape.

Next we demonstrate the impact of geometrical parameters on the temporal shape of the output pulse. Consider the constant lattice, which was previously chosen as $L_x = 200$ nm, $L_y = 100$ nm. For the golden monobar array with $t = 20$ nm and adhered to the fused silica substrate with a 2 nm titanium adhesion, the resonance frequency of the metasurface is kept constant at 370 THz by tuning the width for different lengths of the particle. The compression rate of different metasurfaces are plotted in Fig. 2.4 for the input with a carrier frequency of 370 THz. As this figure indicates, the metasurface filters are able to compress the different Gaussian pulses with different compression ratios. The trend in all cases is the same; the maximum of the compression takes place for a specific pulse width and away from that pulse width the compression ratio decreases. However, as the filling factor of the particle in a unit cell of the metasurface increases, the maximum compression ratio raises. By increasing the filling factor of the particle, the depth of the transmission magnitude increases. The deeper resonance causes the metasurface attenuate stronger center of the spectrum much more than weaker outer parts. Therefore, the bandwidth of the

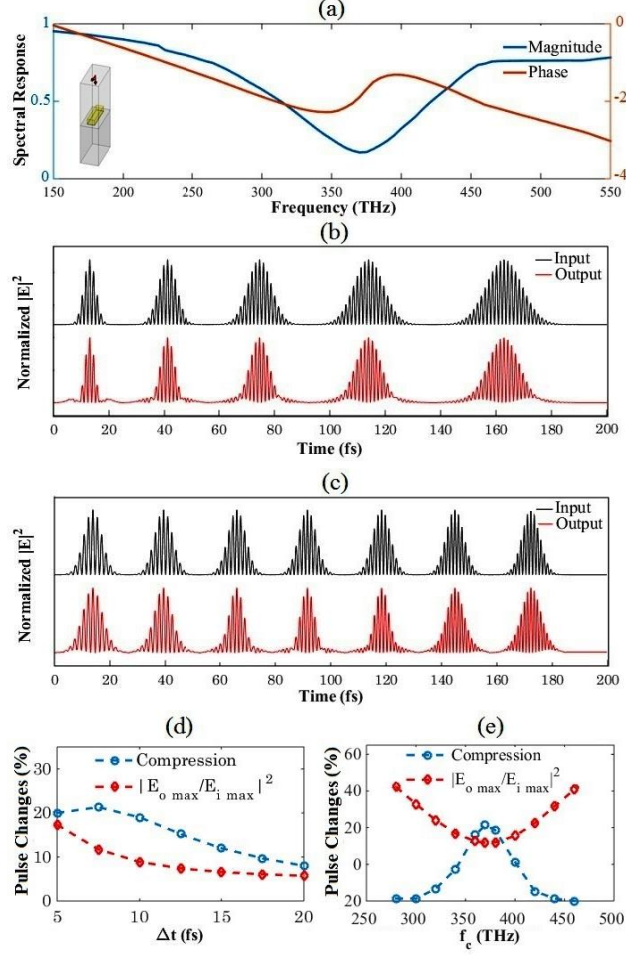


Figure 2.3: Pulse shaping with a golden monobar array, $L = 150$ nm, $w = 50$ nm, $t = 30$ nm, $L_x = 200$ nm, $L_y = 100$ nm, 2 nm titanium adhesion layer on a fused silica substrate. (a) transmission spectral response, (b) input/output comparison for different pulse width at $f_c = 370$ THz, (c) input/output comparison for $\Delta t = 7.5$ fs but different f_c , (d) and (e) compression rate for (b) and (c)

output increases and as a result the compression ratio increases.

2.3 Metasurface Design for Femtosecond Pulse Control

The spectral characteristics of the metasurface transmission determine the temporal shaping of the output signal as discussed in the previous section and Eq. (1). To effectively shape the output signal, a method is developed to design the spectral response of the metasurface, which is detailed in this section. Assume that the input pulse is known and a specific pulse in the output is required. The transfer function of the required metasurface filter can be represented as:

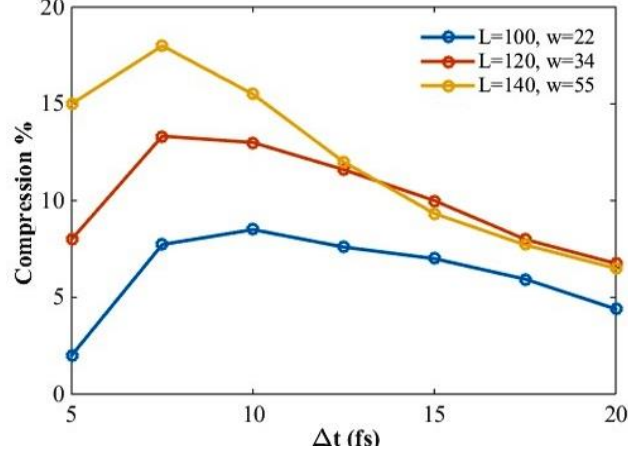


Figure 2.4: Half power pulse width compression of a Gaussian pulse with $f_c = 370 \text{ THz}$ by different metasurface filters. In all cases: $L_x = 200 \text{ nm}$, $L_y = 100 \text{ nm}$ the golden monobar array has $t = 20 \text{ nm}$ and is adhered to the fused silica substrate with a 2 nm titanium adhesion.

$$h(\omega) = \frac{E_o(\omega)}{E_i(\omega)} \quad (2.2)$$

When the denominator is very small in various spectral regions of the input signal, the transfer function $h(\omega)$ will be very large in those spectral regions. In such cases, the design characteristics of the metasurface will be dominated by those spectral regions. To avoid very large responses, the metasurface design can be limited to a frequency band for which the input has a non-negligible spectrum. The multiplication of the input spectrum and metasurface filter's response results in a negligible spectrum error out of this frequency range. To specify this frequency range, the input spectrum can be normalized to its maximum and the range which has a spectrum greater than a threshold is identified as the important frequency range. Then the filter is designed for the frequencies which meet: $|E_i(\omega)| > \delta |E_{imax}|$ that δ is the threshold; hence the intensity is proportional to $|E_i(\omega)|^2 > \delta^2 |E_{imax}|^2$ at the edge frequencies.

This method can be employed to design a spectral response to compress or expand pulses with arbitrary shapes. Here, a Gaussian input pulse is used for both input and output signals. First, the pulse is expanded in the time domain. Based on Eq. 2.5, the

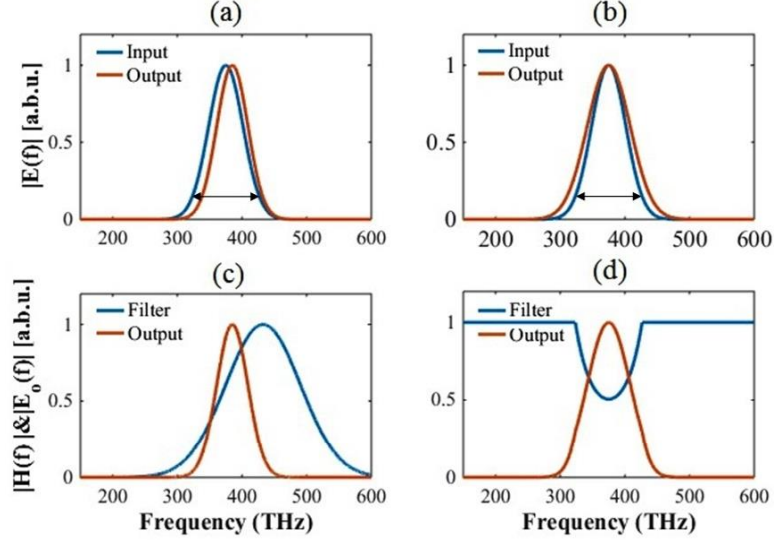


Figure 2.5: Filter design based on input and output spectrum. Gaussian input (blue)/output (red) spectrum in pulse expansion case (a) and in pulse compression case (b). The important frequency range of the input is specified by a double arrow in each subfigure. The filter spectral response (blue) and the normalized filtered output spectrum (red) for pulse expansion (c) and pulse compression (d).

filter has the following frequency response:

$$h(\omega) = h_0 e^{\frac{1}{2}(\omega - \omega_i)^2 \cdot \tau_i^2} e^{-\frac{1}{2}(\omega - \omega_o)^2 \cdot \tau_o^2} \quad (2.3)$$

In this relation, ω_i and ω_o are modulation frequencies of the input and output Gaussian pulses, and τ_i and τ_o are the duration of the input and output pulses, $\tau = \Delta t / \sqrt{8 \ln(2)}$. In this equation, h_0 is a constant, which depends on several parameters including the amplitudes of the input and output pulses. It can be tuned to normalize the metasurface filter's response. To expand the pulse duration $\tau_o > \tau_i$. However, there is no restriction on ω_i and ω_o . By selecting a suitable ω_i and ω_o , the filter can have a monotonic increasing response in the important frequency range which is shown in Fig. 2.5. (a) and (c), so it is simpler to be realized. Similarly for pulse compression we have the condition $\tau_o < \tau_i$. In this case, for $\omega_i = \omega_o$ a wideband dip is required when compared to the previous example. Hence the amplitude of the filter response cannot exceed 1 for passive filters. Therefore, the obtained spectral response is normalized to its maximum in the important frequency range so that it can be realized

using metasurfaces.

An input Gaussian pulse at 370 THz with a 10 femtosecond half power pulse-width is applied to the filter. The objective is to expand the half-power pulse duration by 10%, and next, to compress the half-power pulse duration by 10 %. To design the filter's response, first the important frequency range of input is specified. Considering $\delta = 0.15$ the important frequency range for the described input is between 318.4 THz and 421 THz. To expand the pulse duration by 10%, $\tau_o = 1.1\tau_i$. For this case, the modulation frequency is selected as $f_o = 385$ THz to provide a monotonic and smoothly increasing response in the important frequency range. Based on these parameters, the frequency response of the required metasurface is shown in Fig. 2.5. (c) blue curve. To compress the pulse duration to 10% , $\tau_o = 0.9\tau_i$. For this case $f_o = f_i = 375$ THz. Because the nanoplasmonic filters are passive and they cannot amplify the input, the maximum of the filter's response for this case is 1. As a result, the amplitude response is normalized to the maximum at the important frequency range. The required frequency response of the metasurface is shown in Fig. 2.5 (d) blue curve.

To realize these target filters, two metasurfaces are devised which have quite similar responses to those in Fig. 2.5 within the important frequency band. The thickness of the particles in all cases is 20nm. For the pulse expansion case, the metasurface consists of an array with monobars of length 170 nm and width 50 nm. The periodicity of the structure are 200 nm and 80 nm, respectively. In other words, there is a 30 nm gap in both directions between the monobars. The structure is stimulated by a linear polarized plane wave which impinges perpendicularly on the array surface and the polarization is parallel to the length of the monobars. The corresponding transmission spectral response of the structure is shown in Fig. 2.6(a). Next, for the pulse compression case, the structure is realized by a multi-resonant metasurface. While the single nanoparticle arrays may offer limited bandwidth, multi-resonant structure is much versatile to make wider dip spectral line-shapes. Therefore, it tailors the temporal profile of the femtosecond pulse much precisely. Here, the unit cell includes 6 bare-shaped nanoparticles which provide different resonances; they are distributed almost evenly on the

unit cell's substrate to decrease any inter-particle effects. The filling factor is devised for 50 % transmittance at resonance as Fig. 2.5 (d) offers; therefore, the length and width of the cell are chosen 500 nm and 250 nm respectively. The lengths of particles are chosen differently but close to each other so that the overall spectral line-shape have a combined wider dip. All the particle are oriented in the length of the array and have 30 nm width. The lengths are 86,96 ,103, 103, 110 and 118 nm, and their center point is located respectively in [-125,-83], [125,83], [0,0], [250,0], [-125,83] and [125,-83]. These 6 structures are repeated periodically. The corresponding transmission spectral response for the pulse compression case is shown in Fig. 2.6 (b).

These two metasurfaces are used for pulse expansion and compression. Multiplying the obtained spectral response with the input spectrum results in the output spectrum. Taking an inverse Fourier transformation gives the time domain output pulse. As expected, the output shapes which are compared to the input pulses in Fig. 2.6. (c) and (d) have shapes that are quite similar to the Gaussian form. In Fig. 2.6. (c) the normalized temporal profile of the output intensity is expanded. The half power pulse width of the output is increased by 11.5 %, which exceeds the targeted 10 % increase. For the pulse compression case: Fig. 2.6(d) indicates that the output pulse is compressed by 9%. These variations from the target are due to the differences in the targeted transmission spectrum and the realized transmission spectrum using the metasurface. Nonetheless, the metasurface filters are capable to compress and expand the pulse shape without any deshaping or sidelobes.

2.4 Polarization Control of Femtosecond Pulses

Since the transmission response of the metasurfaces is polarization dependent, it can be employed as a polarization shaper for ultrashort pulses. Here, it is shown that this filter alters the polarization of the incident linearly polarized pulse after passing through the metasurface.

Fig. 2.7 demonstrates the metasurface's ability to transform the polarization of the

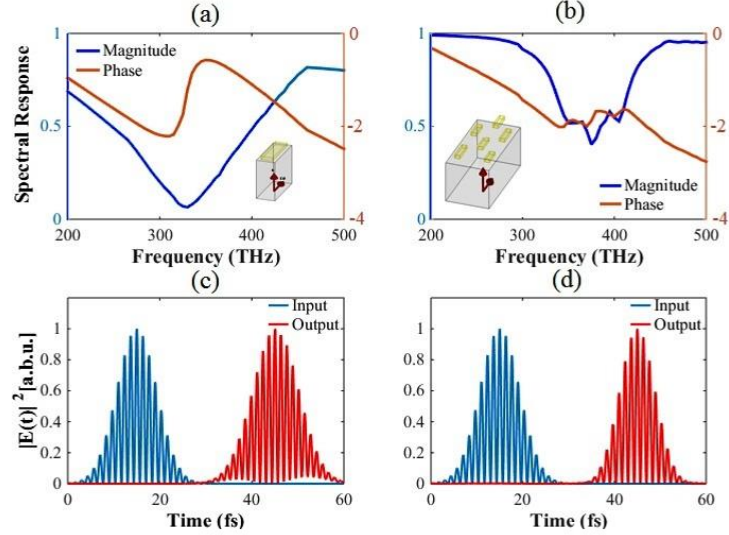


Figure 2.6: (a) and (b) realized filters spectral amplitude (blue) and phase (red) response for the designed responses of Fig. 2.5. (c) and (d); comparison of the normalized input and output pulses, (c) pulse expansion case and (d) pulse compression case.

incident pulse. A golden monobar array with $L = 100$ nm, $w = 30$ nm, $t = 30$ nm, $L_x = 120$ nm, $L_y = 100$ nm and a 2 nm titanium adhesion layer on fused silica is used in the simulations. The transmission response of the metasurface is plotted in Fig. 2.7 (b) and (c) for different input polarizations. These subfigures indicate that $f = 405TH$ is an appropriate input frequency because the phase difference of the two transmitted components in this frequency is closer to $\pi/2$. The input polarization is then tilted by 18° from the x axis in order to set the amplitude ratio of the transmitted components. Fig. 2.7 (d), (e) and (f) indicate the output pulse for the Gaussian input of durations 10fs, 20fs and 30fs. In the insets the output field component dependencies to each other and to time is shown too. As seen, the output polarization is no longer linear and the metasurface altered the output polarization in time dependent manner. As the input duration increases the output pulse becomes closer to a circular polarized pulse. The reason is that by increasing the pulse duration, its bandwidth decreases; by decreasing the bandwidth the pulse experiences a smaller spectrum variation imposed by the filter. Not only the polarization but also the pulse shape and duration of output pulses are changed by the filter. For instance, for 10 fs input pulse, output intensity duration is 6.8 fs which is 32% shorter than the input duration. The 30 fs input pulse

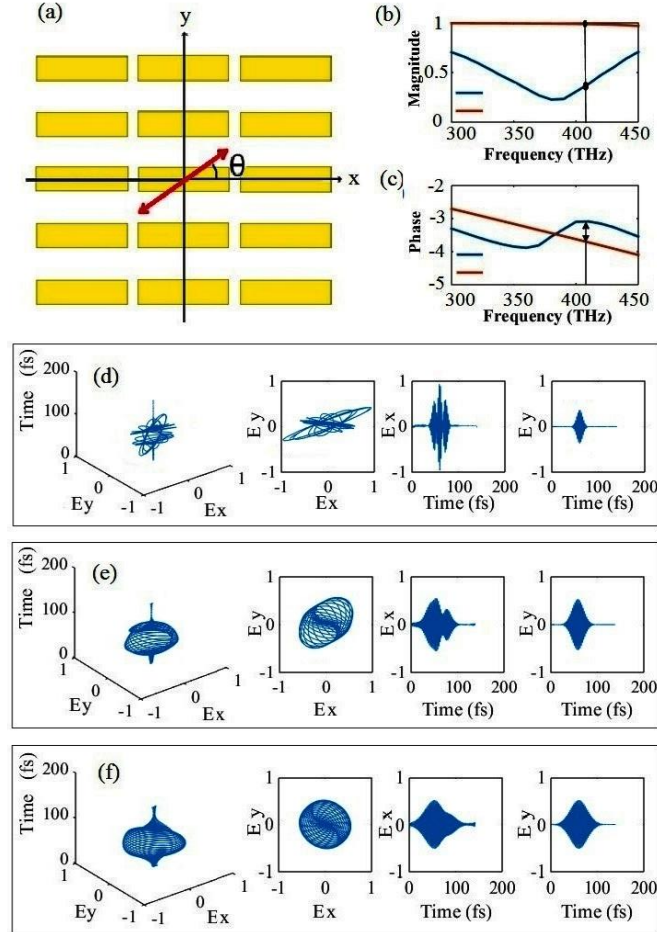


Figure 2.7: Linear to circular polarization conversion of the ultrafast pulse by the metasurface. (a) the metasurface and tilted linear-polarized input, (b) magnitude and (c) phase of the transmission for a golden monobar array with $L = 100$ nm, $w = 30$ nm, $t = 30$ nm, $L_x = 120$ nm, $L_y = 100$ nm and a 2 nm titanium adhesion layer on fused silica. (d), (e) and (f) the polarization shaped pulsed Gaussian pulse of durations 10fs, 20fs and 30fs

is transformed to 33.5 fs pulse at the output which is 11.5% wider. Therefore, as the input duration increases the output duration undergoes less changes due to smaller spectrum variation imposed by the filter. Hence the output pulse is not necessarily smooth and may have side lobes as of Fig. 2.7 (d).

2.5 Reconfigurable Metasurface

It is shown that a metasurface composed of nano-particles supporting LSPs, can be employed as a band-stop spectral filter to manipulate the temporal properties of an

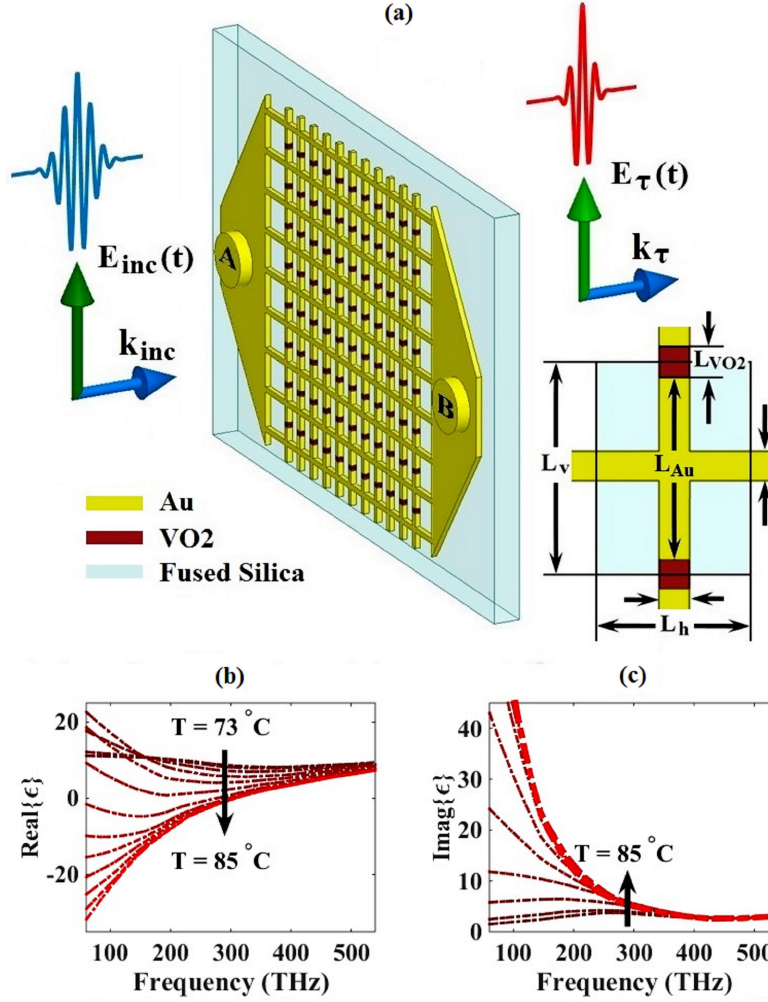


Figure 2.8: (a) Dynamic pulse shaping schematic by reconfigurable localized surface plasmon based on insulator to metal phase transition of VO2. (b) real and (c) imaginary parts of VO2 relative permittivity changes by temperature. The darkest red shows the material property at 73 °C and brighter reds represent the property at higher temperatures up to 85 °C

optical transmitting wave. The band-stop lineshape can be manipulated through the particle geometry variation as demonstrated. In this Section, the lineshape adjustment is applied by controlling VO2 material phase in the metasurface lattice through controlling its temperature. VO2 temperature setting is obtained by Joule heating of the structure as shown in schematic of Fig. 2.8 (a).

An applied voltage across points A and B causes a current flow in the metallic lattice which generated resistive heat to set VO2 temperature. The permittivity of VO2 changes accordingly and alters the resonance of vertically oriented metallic bars with

vertically polarized light. The existence of horizontal interconnects for Joule heating slightly changes this resonance by shifting its frequency, however, this part of the lattice seems almost transparent to the vertical polarized light. The thermal variation of VO2 spectral permittivity is depicted in Fig. 2.8 (b) and (c) across the phase transition by a spline interpolation of the experimental data from the literature [111]. To avoid VO2 permittivity ambiguities due to hysteresis [112,113], the obtained data upon heating is reported and used here. Photo-induced phase transition in VO2 is eluded by setting the fluence of the input pulse below a certain threshold which depends on factors such as ambient temperature and VO2 thickness [112,113]. Furthermore, VO2 charge-induced phase transition does not take place here because the heating current passes thorough horizontal metallic bars but not VO2 cubes due to the direction of applied voltage in the proposed configuration of Fig. 2.8 (a).

Because of finite conductivity of the metal, applying a DC voltage across terminals A and B in Fig. 2.8 (a) results in power loss inside the lattice in the form of heat. The overall generated heat power can be approximated by $H_{in} = (V_A - V_B)^2/R_{equ}$ which R_{equ} is the equivalent resistor between terminals A and B. The current flows evenly among the identical inter-terminal metallic horizontal bars, as a result, their resistances are parallel and $R_{equ} \cong R_{hb}/n$ where R_{hb} is the resistance of each horizontal bar, n is the number of them and terminals resistances are neglected. The resistance of each horizontal bar is given by $R_{hb} = l/(\sigma.A_{CS})$ where l is the length of the bar, A_{CS} is its cross section area and σ is the bulk conductivity of the metal. The attached vertical metallic bars carry no voltage-induced current and so they have negligible effects on R_{hb} . Assuming averaged natural convective cooling rate of $h_{av} = 5 W/(m^2K)$ [114] by surrounding air at T_{amb} the heat conduction at substrate glass and the lattice metal takes place at a much higher pace for milliliter size structure [115] while thermal radiation to air and heat conduction through terminals and fixtures are considered negligible. Therefore, after becoming isothermal, temperature raises exponentially all over the structure to reach an steady state when the rate of lost heat by air equals the rate of generated heat in the lattice. Supposing an structure consisting of fused silica

substrate of $3\text{mm} \times 3\text{mm} \times 0.5\text{mm}$, a gold lattice of $1\text{mm} \times 1\text{mm} \times 20\text{nm}$ located on top of it, the unit cell with $L_v = 140\text{ nm}$, $L_h = 100\text{ nm}$, $L_{Au} = 130\text{ nm}$, $L_{VO_2} = 10\text{ nm}$, $w=20$ and the gold bulk conductivity of $\sigma_{Au} = 4.1 \times 10^7$ [116], one can obtain $R_{hb}=60.1\text{ k}\Omega$, $n=7143$ and so $R_{equ}=8.54\ \Omega$. The resistance changes with temperature due to conductivity variation of gold are neglected here for the sake of simplicity. In the steady state $H_{in} = H_{out} = h_{av} \cdot A_t \cdot (T_{ss} - T_{amb})$ which A_t is the total area of the structure and T_{ss} is the steady state temperature. Therefore:

$$T_{ss} = T_{amb} + \frac{(V_A - V_B)^2}{R_{equ} \cdot h_{av} \cdot A_t} \quad (2.4)$$

Note that the filter structure is approximately isothermal and so $T_{VO_2} = T_{ss}$. This equation then relates driven voltage and VO2 temperature logically at steady state; it can be easily calibrated to set up VO2 temperature in the metasurface lattice precisely.

Thereafter, temporal response of the metasurface is extracted by calculating spectral transmission coefficient through the lattice upon normal incidence of light for different temperatures. A commercial finite difference time domain code [117] is employed to model the optical response of the proposed structure numerically. Also, it is assumed that the rear side of the substrate is covered by perfect anti-reflective coating.

The impulse response of this metasurface can comprehensively characterize its optical filtering properties, because the metasurface is time invariant in the time-scale of each experiment (constant VO2 temperature in steady state) and the transmission through it is a linear function of the input pulse for the pulse fluences far below 1 mJ/cm^2 [113]. The impulse response can be calculated for a logical range of frequencies by applying a wide-band input pulse to the metasurface and measuring the transmitted output pulse. Spectral representation of the approximated transmission coefficient impulse response is then $h(\omega) = E_o(\omega)/E_i(\omega)$. Once the spectral response of a metasurface is obtained it can anticipate the transmitted optical pulse for any arbitrary input temporal profile using Fourier analysis.

Depending on the LSP and VO2 particles are associated in metasurface, the thermal

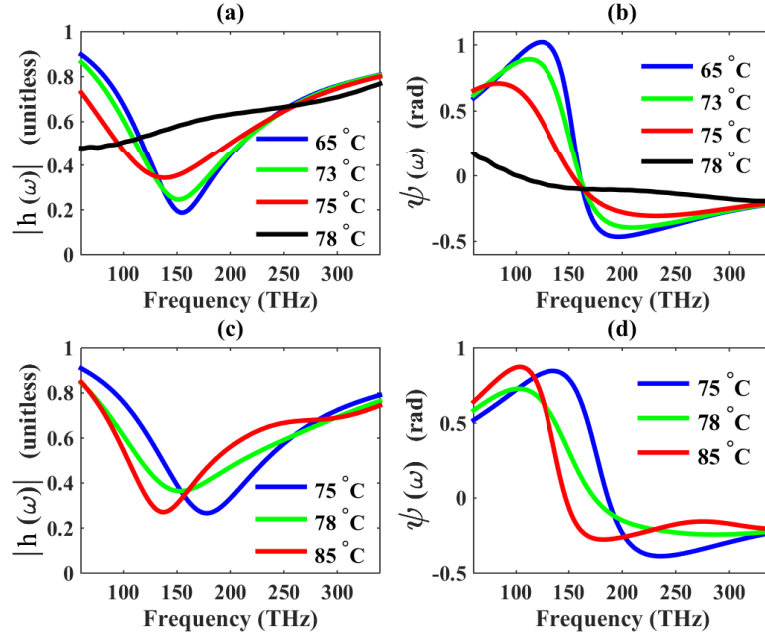


Figure 2.9: Transmission coefficient's amplitude (a) and phase (b) of a metasurface devised for thermal controlling of band-stop optical filter's dip strength in several temperatures. Transmission coefficient's amplitude (c) and phase (d) for a metasurface with thermally controlled stop frequency filtering in different temperatures.

control can primarily manipulate either resonance depth or resonance frequency of transmission coefficient lineshape. In the former case, VO₂ is employed to govern the loss rate of LSP resonances; however in the latter case, VO₂ particles add/deduct the length of the LSP resonators by transforming interconnections of two or more LSPs to metallic/insulator. Both of the methods are illustrated by appropriate examples.

To employ VO₂ as dip controller of $h(\omega)$, the illustrated configuration of Fig. 2.8 (a) with the previously mentioned dimensions can be employed. The vertically oriented localized surface plasmons are interconnected through VO₂ nano-particles and are placed on top of the transparent fused silica substrate. The longer horizontal bars do not affect the lattice resonance effectively since it is excited with perpendicular polarization. The structure can be fabricated using conventional electron beam lithography techniques [118, 119]. Spectral transmission coefficient of this metasurface is shown in Fig. 2.9 at different temperatures. The amplitude of $h(\omega)$ is shown in Fig. 2.9 (a) and corresponding phase is represented in Fig. 2.9 (b). As shown in the former, in lower temperatures the structure attenuates transmitted spectrum around a specific

resonance frequency while it passes the rest of the spectrum almost unattenuated. The attenuation is caused by frequency-selective localized surface plasmon resonances of free electrons inside gold nano-particles and associated losses. The dip lineshape of transmission can be modeled by Fano-type resonance [74]:

$$h(\omega) = |h(\omega)|e^{j\psi(\omega)} = h_0 + \frac{Se^{j\phi}\Gamma}{\omega - \omega_0 + i\Gamma} \quad (2.5)$$

In Eq. (2.5) h_0 is the nonresonant transmission amplitude, $Se^{j\phi}$ is the oscillator strength, ω_0 is the resonance angular frequency and Γ is the frequency width of LSP resonance. The variables of this equation can be adjusted in order to fit Eq. (2.5) to the obtained transmission coefficient from numerical results for each temperature. By temperature increment, the band stop dept of S diminishes and the resonance frequency ω_0 shifts to the lower bands. In higher temperatures, VO2 transform to a lossy metal which can conduct the free electrons of gold. Consequently, surface plasmons tend to propagate rather than resonate locally. In $T = 78^\circ C$, the resonance disappears and the filter passes all the spectrum with moderate attenuation. Spectral phase of transmission coefficient $\psi(\omega)$ for a sample metasurface at different temperatures is shown in Fig. 2.9 (b). This phase also obeys from the phase relation of Eq. (2.5) once the parameters are fitted for the amplitude match. For weaker resonances in higher temperatures, filter's phase response has smoother variations. Nonetheless, for stronger resonances in lower temperatures, filter's phase response has sharper variations.

To control the resonance frequency of $h(\omega)$ without considerable affecting dip strength, the shown configuration of Fig. 2.8 (a) with slight changes can be utilized. If VO2 cubes of even rows of VO2 in the lattice are substituted by air gap, the structure functions as mentioned. This way, each 2 vertical gold bars make a resonating system while the VO2 interconnect is metallic; they become segregated resonators when VO2 is an insulator. Fig. 2.9 (c) and (d) show the transmission coefficient variation of such a filter with temperature for the following dimensions: $L_v = 120$ nm, $L_h = 100$ nm, $L_{Au} = 114$ nm, $L_{VO2} = 6$ nm and $w=20$ nm. The figure points out that the resonance frequency of h is decreased by 30 % due to temperature increment from $75^\circ C$ to $85^\circ C$ and

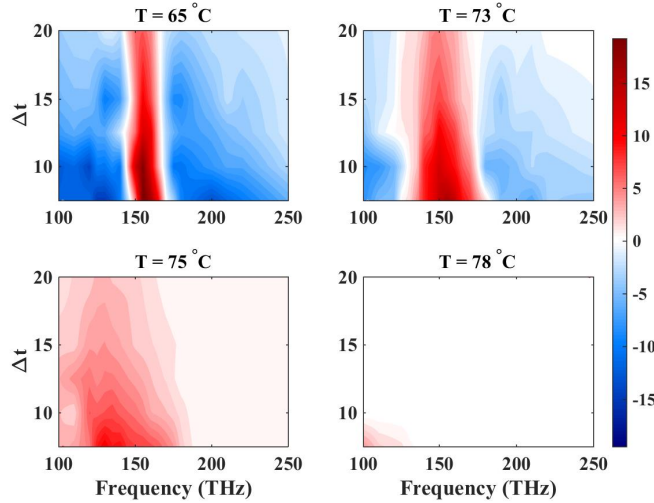


Figure 2.10: Half-power pulse span compression (red) and expansion (blue) percentage for various pulses with variable carrier frequencies and spans at different temperatures

the general band-stop lineshape trend is approximately unchanged. While transition between these temperatures, the resonance strength S decreases and bandwidth Γ increases because VO2 at these temperatures neither is a low-loss insulator nor is a good metal and therefore it adds to the loss rate of the resonators, resulting the mentioned change of the lineshape.

2.6 Dynamic Pulse Shaping

As the proposed reconfigurable filters can tailor the spectrum of the transmitted pulse, the temporal characteristics are also changed during this process. Depending on the temporal characteristics, pulse can be shaped in different ways. In this section, we investigate the configuration of Fig. 2.9 (a) and (b). The percentage (%) of half-power pulse span compression and expansion of this filter at transmission is shown in Fig. 2.10 in different temperatures for an incident light with Gaussian temporal profile.

The red color in Fig. 2.10 specifies the pulse compression and blue one shows the pulse expansion. At $T = 65\text{ }^\circ\text{C}$, the filter has a strong dip around 150 THz which can compress pulse span up to 20 % (widen its spectrum by selective attenuation of spectrum peak) for pulses with carrier frequencies close to this resonance. This ability decreases as the pulse span increases because the spectrum becomes narrower

comparing to the filter width (Γ). For pulses with carrier frequencies out of 145-165 THz band, the passing pulse through the filter undergoes expansion. The reason behind this phenomenon is that the dip at 150 THz make the passing spectrum narrower; therefore, based on Fourier analysis pulse width increases. The percentage of pulse expansion is higher for shorter pulses with moderately closer carrier frequencies. At carrier frequencies far away from the filter resonance, all the spectrum passes through it almost unchanged and so the pulse expansion decreases. The same pattern is repeated for $T = 73 \text{ }^\circ\text{C}$; however, due to weaker resonance strength (S) of the filter the pulse compression/expansion ratios are decreased. Furthermore, because the filters spectral width (Γ) is increased in this temperature, the compression frequency range is broadened to 130-170 THz. As the temperature raises to $T = 75 \text{ }^\circ\text{C}$ the ability of the filter to expand the pulse span fades and its pulse compression ratio diminishes. Finally at $T = 78 \text{ }^\circ\text{C}$ the pulses pass through the filter with very negligible shape changes except amplitude attenuation. Indeed, the intensity attenuation takes place in all the above cases due to passiveness and linearity nature of the pulse filtering ; it can be as intense as $|h_0 + S \times \exp(j(\phi - \pi/2))|$ which is the transmission amplitude at resonance.

On the other hand, the filter with variable dip can be a delay controller line for narrow-band pulses. In frequency ranges close to the resonance frequency, transmission coefficient amplitude has small variations. Additionally the phase is a linear function of frequency. As a result, the transmission coefficient can be approximated by $|h(\omega_0)|e^{j(\psi_0 - \omega t_0)}$ which can make a delay to the pulse propagation for a fitted t_0 :

$$\begin{aligned} E_o(t) &= F^{-1}\{|h(\omega_0)|e^{j(\psi_0 - \omega t_0)} E_i(\omega)\} \\ &= |h(\omega_0)|e^{j\psi_0} E_i(t - t_0) \end{aligned} \tag{2.6}$$

Therefore, the slope of phase $\psi(\omega)$ in this frequency band is the amount of delay time applied to the transmitted narrow-band pulse in addition to its propagation delay time. For the devised metasurface with characteristics of Fig. 2.9 (a) and (b), depending on the temperature of the structure, the delay time can change as shown in Fig. 2.11. This figure suggests that variable delay up to 8 femtosecond can be applied to the

pulse. This time delay is negligible comparing to picosecond timescale of IMT in VO₂; However, it can be employed to tune delay time between different pulses or waves. Particularly because the period of 150 THz light is 6.67 femtosecond, variable delay by the filter can facilitate optical phase shifting up to $360^\circ \times 8/6.67$.

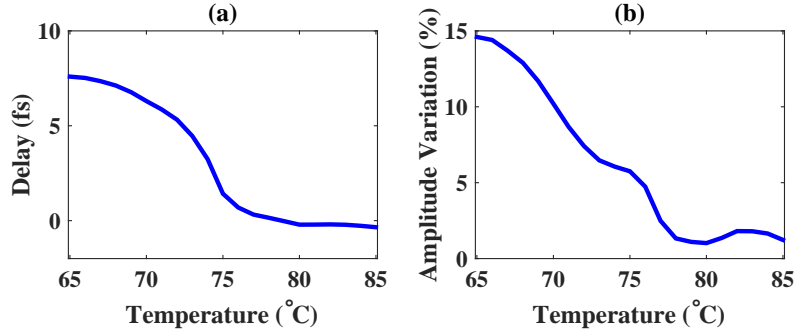


Figure 2.11: (a) The transmission coefficient phase slope represented in the form of a narrow-band pulse delay versus temperature at 150 THz for optical filter of Fig. 2.9 (a and b). (b) Maximum amplitude variation of the transmission coefficient in 150 THz $\pm(5\%)$ range.

The transmission coefficient phase is linear in a limited range of frequencies around the resonance. In this band the transmission coefficient amplitude undergoes smooth spectral variation. To have an idea of the amplitude variation of the filter around resonance, this property is calculated for the range of 142.5 THz to 157.5 THz (10 % bandwidth) and plotted in Fig. 2.11 (b). This figure shows that to apply bigger delay times to the pulse, small spectral distortion may be applied to the signal by smooth amplitude variations of the pulse up to 15 %.

Monolayer metasurface can assess moderate spectral selective attenuation which may restrict the pulse manipulation to limited pulse span changes. In order to provide versatile pulse shaping by higher spectral selective attenuations, multilayer parallel metasurfaces can be employed. However, in normal incidence of input pulse, multi-reflections between metasurfaces may cause deterioration of filter performance. In this case, by oblique incident one can get rid of the reflection spectrum and obtain identical transmission to that one of the normal incidence condition as long as the distance between the layers is set carefully to avoid reflections in the filtered light. Hence that the grating reflection modes cannot be excited for short lattice constants as it is the case here.

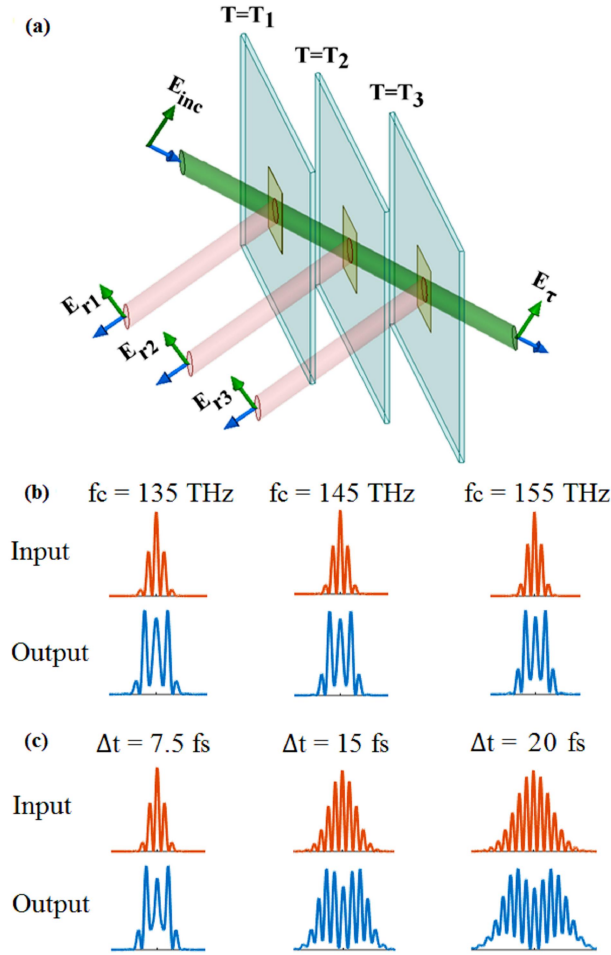


Figure 2.12: (a) Multilayer parallel metasurfaces with independent thermal controls which oblique incident angle and appropriate distance between the metasurfaces avoid multi-reflections to the output. Pulse shape preservation for variable carrier frequency (b) and variable pulse span (c) using the configuration shown in (a).

By setting the metasurfaces temperature of each layer differently from each other, a trilayer metasurface as shown in Fig. 2.12 (a) can facilitate a fully temperature controlled pulse shaper for a range of pulses. For instance, if two top layers are filters with performance of Fig. 2.9 (a) and (b), also the bottom (third) layer is the filter with performance of Fig. 2.9 (c) and (d), by setting layers temperature $T_1 : T_2 : T_3$ preservation of pulse shape (widened by 90 %) in different conditions is shown. If the carrier frequency of input Gaussian pulse changes, reconfigurability of the filter compensate the change to preserve the pulse shape similar as seen in Fig. 2.12 (b). The metasurface temperatures in degrees of Celsius are 73:78:85, 65:78:78 and 73:78:75

for corresponding carrier frequencies of 135 THz, 145 THz and 155 THz. If the span of input Gaussian pulse changes, filter compensate the change to preserve the pulse shape and expansion rate as illustrated in Fig. 2.12 (c). The metasurface temperatures in degrees of Celsius are 70:78:78, 65:73:78 and 65:65:78 for corresponding pulse spans of 7.5 fs, 15 fs and 20 fs. In all the above cases the pulse half-power span is widened by 90 %. The configuration is also able to provide wider phase shifts up to $3 \times 360^\circ \times 8/6.67$ for narrow-band pulses because the transmission phase of layers are added to make a steeper overall transmission phase in the resonance region.

2.7 Conclusion

In summary, a compact and ultrathin plasmonic metasurface was demonstrated for ultra-short pulse shaping in the transmission mode. The metasurface is capable of broadening, compressing, and reshaping the polarization of ultrashort pulses with great control over its characteristics by engineering the resonances of the ultrathin plasmonic metasurface. Furthermore, a reconfigurable localized surface plasmon based spectral band-stop filter driven by IMT of VO₂ was. A Joule heating mechanism that is transparent to the polarization of incident pulse was proposed to control the thermal phase transition of VO₂ and corresponding voltage-temperature equation was extracted. The thermally controlled phase transition of this material enables tailoring the band stop transmission response of the filter in two different ways. The study illustrated that if VO₂ phase transition add/deduct the loss of the system, it can alter the strength of localized surface plasmon resonance which affects the filter's transmission depth. By controlling temperature it was shown that filter varies between band-stop state and all-pass form using a finite difference time domain solver of Maxwell equations. On the other hand, metalization/demetalization of VO₂ interconnect between two localized surface plasmon can lengthen/shorten their effective length and so alter their resonance frequency.

Using this reconfigurable optical filter, shaping femtosecond scale optical pulses

was studied. The effect of temperature variation on the Gaussian pulse span was characterized using Fourier analysis. The filter can give a variable response depending on how the input spectrum is located comparing the resonance of the filter. Pulse span compression/expansion ratios up to 20 % was achieved by single metasurface. Moreover, the filter facilitated a flexible delay line or phase shifter to narrow-band input with less than 10% bandwidth. Then to provide much functional and versatile pulse shaper with grater abilities to compress/expand pulse span a multilayer structure was proposed. It was shown that the metasurfaces temperatures can be tuned to compensate input wanted/unwanted carrier frequency shifts and pulse span variations to preserve the output pulse shape and duration.

Chapter 3

Switchable Plasmonic Yagi-Uda Antenna

3.1 Introduction

Optical antennas have attracted significant interest for intrachip micro/nano scale communication because of large metallic absorption loss of their rival i.e. plasmonic waveguides [120]. Spatially selective wireless communication is achievable using directive antennas [121] and nano-plasmonic Yagi-Udas are able to provide this quality in the optical regime [122–128]. Dynamically switching the antenna radiation enables a communication system to function as a reliable nano-scale switch for signal handling [129–131], modulation [132, 133] and information processing [134–136]. Various techniques have been used for real-time control of nano-antenna radiation patterns. These works include a bimetallic plasmonic dimer [137] and dielectric pairs [138] for switching radiation directionality. In the literature, it has been demonstrated that the metal nonlinearity enables directionality manipulation by adjusting the input power of the antenna [40–42]. Likewise, semiconductor nonlinearity can control the tuning of a plasmonic optical Yagi-Uda antenna in a range of wavelengths [43]. At the same time, selective thermal control of optical antennas can be used to steer the angular responsivity [139], when the antenna thermal switching is provided by current-driven Joule

heating [140]. Although these methods provide some degree of switching over antenna directionality and radiation rate, practical designs and further control over mentioned factors are desirable for chip applications.

Phase change materials have been shown to tailor optical phenomena through an impact on the refractive index of the physical system by an appropriate external stimuli [20,26,100,141–143]. Vanadium dioxide is a good example of a PCM as it undergoes a saturating but reversible insulator to metal phase transition by heating from room temperature ($30\text{ }^{\circ}\text{C}$) up to $85\text{ }^{\circ}\text{C}$ [10,93,97–99]. The IMT has been exploited for plasmonic applications through its effect on the resonance frequency of localized surface plasmons [24,28,100,101]. Picosecond scale transition time of the material [96] is a good reason to use it in ultrafast devices. Recently VO₂ has been utilized to control scattering beam of slot arrays [144] as well as surface waves directional scattering of plasmonic patches [145]. Apart from scatterers, general term PCM has been suggested for controlling the radiation direction of quantum emitters by switching the host material refractive index surrounding a near cut-off Bragg plasmon chain [146].

In this chapter, a switchable-beam Yagi-Uda antenna which is enabled by a thin layer of VO₂ is proposed and then analyzed. The highly directional vertically polarized antenna at room temperature is able to be switched to a low-gain non-directional emitter by raising its temperature by $85\text{ }^{\circ}\text{C}$. The change in VO₂ optical properties due to temperature variation [97] alters the loss rate and shifts the resonance wavelength of antenna elements. The increased loss diminishes antenna radiation while the resonance shifts cause a change in relative phases of the antenna elements; hence it changes directionality of the antenna. Consequently, the phase transition can change the antenna radiation pattern between a strongly radiative directive mode and a weakly radiative non-directive state. The pattern variations are investigated and compared to that of the isolated feed radiator using a full-wave solution of Maxwell’s equation. The changes are explained by analyzing induced currents in the elements and their comparative variation with the phase transition of VO₂. Since the antenna can be fabricated using conventional lithography techniques and has switchable strong vertically polarized

azimuth radiation, it is suitable for integrated optical communicating chips [147].

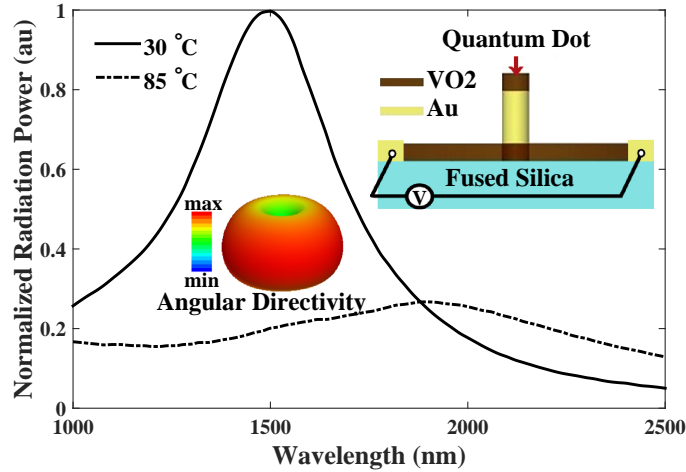


Figure 3.1: Normalized spectral radiation power (integrated over all 4π steradians for each frequency) of a QD fed single radiator at $30^{\circ}\text{C}/85^{\circ}\text{C}$. The radiator antenna consists of a gold cavity cylinder of length 275 nm and diameter of 100 nm which is covered with 70 nm of VO2 coating. The voltage across VO2 causes heating by current flow and adjusts temperature. Antenna radiation pattern is shown in linear scale at resonance i.e. $\lambda = 1500$ nm, $T = 30^{\circ}\text{C}$.

3.2 Isolated Radiator

To understand its role in a Yagi-Uda antenna array, we first studied an isolated feeding radiator switched by PC material. Here, a vertical set-up is selected for the orientation of the nanoantenna structures, which provides vertical polarized radiation. This polarization better persists in ground plane losses and propagates to longer ranges on the chip compared to horizontal polarization [148], which can be obtained by a horizontally aligned dipoles [123]. Despite fabrication challenges related to the vertical set-up, it was preferred due to the advantages in terms of losses and propagation distance, which are desired for applications with lossy substrates. The isolated feeding radiator consists of a vertical metallic cylinder on top of a dielectric substrate as shown in the subset of Fig. 3.1. This structure is exposed to a thin layer of VO2 coating and a tiny quantum dot (QD) is placed on top of a VO2 cylinder located on the rod's topmost point. Metallic cylinder on dielectric substrate can be fabricated using conventional techniques i.g. electron beam lithography. Then a polycrystalline VO2 coating can be added on top of the structure by magnetron sputtering using V2O5 target and the introduction of

oxygen or hydrogen gases [149]. The polycrystalline lattice constant [150] is close to that one of the cylinder metal and the substrate which ease deposition of VO₂ thin layers on top of these materials with negligible roughness. VO₂ temperature can be adjusted by applying a tunable voltage across the VO₂ on the substrate by a pair of probes [151, 152] as shown in Fig. 3.1 subset. As a result, a current passes through VO₂ and heat up the structure. By lowering the current, VO₂ temperature decreases and the structure cools down. Due to the high thermal conductivity of metallic nano-rod [153], the topmost VO₂ nano-cylinder follows the temperature of the VO₂ on the substrate. The QD can be added to the structure by a combined top-down fabrication and bottom-up assembly. Electron beam lithography provides a chemical binding site on top of the nano-rod that is buried in photoresist. Then a series of surface chemical functionalization processes allow the programmed assembly of a colloidal quantum dot e.g. CdSe in the specific area [154]. After removing the photoresist from the structure, a vertically polarized low power laser can illuminate the QD to excite radiation without affecting the phase of VO₂ [155].

Vertically polarized QD oscillation vibrates free electrons in the metallic cylinder vertically, which generates a current inside it. The induced current facilitates omnidirectional radiation especially when the structure resonants [123]. PC in VO₂ affects the radiation efficiency through two phenomenons. First, the PC impacts the induced current strength mainly controlled by the topmost VO₂. Second, the PC shifts the resonance wavelength of the system. A combination of the aforementioned factors switches the spectral radiation line-shape of the antenna. Weak resonance is expected from the system at higher temperatures due to losses imposed by the metallic VO₂. However, at room temperature VO₂ is a low loss insulator, hence stronger resonance and radiation are expected.

To study the antenna numerically, a commercial finite element solver of Maxwell's equations (HFSS) is employed [156]. Fused silica which is a transparent dielectric at visible and near-infrared wavelengths is chosen as the substrate and gold is selected as the plasmonic resonator metal. Optical properties of gold, polycrystalline VO₂ thin

film and fused silica are taken from experimental reports [97, 108, 109]. To excite the antenna, a tiny vertical voltage source which models a pure electric dipole transition QD is utilized [157]. The device is designed to resonate at the infrared regime due to the high contrast of VO₂ properties in both the insulator and metallic phases at those wavelengths [100]. The length to diameter ratio for the nano-rod has to be kept small enough to avoid the fabrication difficulties of vertically oriented high aspect ratio cylinders. In addition, the VO₂ thickness has to be thin enough to adhere to the top of the Au cylinder firmly. Furthermore, it has to be thick enough to cause switchability of the antenna. Optimizing the antenna length numerically for a diameter of 100 nm and an exposed VO₂ thickness of 70 nm aiming for the first resonance at $\lambda = 1500$ nm results in $L_{Au} = 275$ for the metallic rod. The antenna has a broad spectral response as depicted in Fig. 1 because it is a relatively thick antenna [158]. When the temperature switches to 85 °C, the antenna resonance attenuates and shifts to 1950 nm. The optical index of polycrystalline VO₂ at 30 °C and $\lambda = 1500$ nm is $3.25 + i0.28$ while it turns to $1.89 + i2.62$ at 85 °C which is much lossy but still metallic. Gold index at this wavelength is $0.53 + i9.51$. The normalized radiation spectrum of the antenna at both temperatures are shown in Fig. 3.1. This figure shows that the maximum spectral radiated power of the antenna at 30 °C is almost 3 times stronger than that of the radiated power at 85 °C. Nonetheless, the radiation pattern remains omni-directional for both resonances (the pattern at $\lambda = 1500$ nm is depicted here). Furthermore, the antenna at high temperature has negligible frequency selectivity. This result indicates a weak switchability of the radiation pattern through engineering the resonance wavelength via PC material in this configuration.

3.3 Isolated Scatterer

To understand the thermally-induced pattern variation of the Yagi-Uda antenna array, the impact of the parasitic elements scattering and their changes with temperature are studied. If the excitation and the induced currents are known over the parasitic

elements, the antenna radiation pattern can be predicted through antenna array analysis [159]. For example, to have an element which reflects the power, the induced current phase on the element must be in the range of 0 to 180° when compared to the driven element phase. On the other hand, if the current phase of the element is between 180° and 360° , it can direct the radiated power from driven element. The spectral variation of the induced current in the center of the parasitic element when they are excited by a vertical-polarized traveling plane wave is calculated and shown in Fig. 3.2.

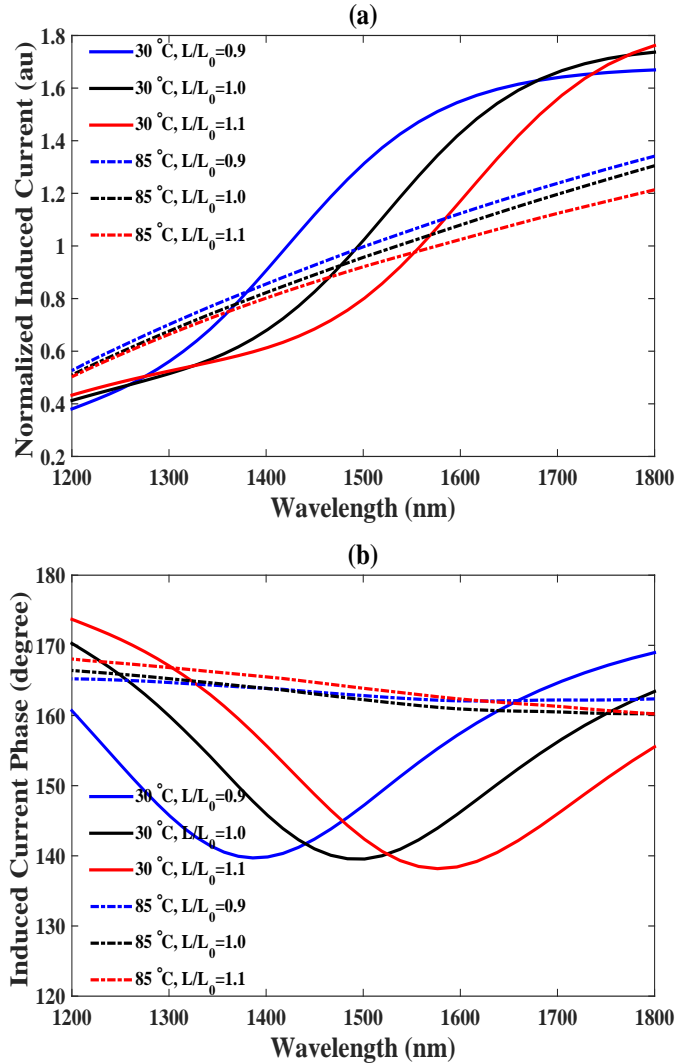


Figure 3.2: Spectral comparison of induced current at the midpoint of the gold nano-rod due to plane wave incidence for different rod lengths and temperatures. (a) normalized amplitude and (b) corresponding phase with reference to the incident electric field phase.

The incident wave on the nano-rod induces a current on it, which increases by

increment of wavelength. The current profile shifts in frequency by changing the nano-rod length as the effective light wavelength in gold is changing almost linearly by frequency in this range of wavelengths [9,160]. The induced current in gold cylinder experiences sharper spectral variation around a specific wavelength at 30 °C as Fig. 3.2 (a) demonstrates. The current phase drops to its minimum at this wavelength. On the other hand, the induced current in the gold at 85 °C changes smoothly with no resonance.

The spectral phase variation of the currents is shown in Fig. 3.2 (b). The induced current phases of devised gold rod at high temperature are a bit different than that one of an infinity long cylinder which is 180 degrees out of phase with reference to the incident electric field; nonetheless, it has negligible phase variation. Although at 85 °C the lossy metallic VO₂ prevents the current from resonating sharply, it alters the phase of the induced current by 12-18 degrees from 180°. On the other hand at lower temperature, the spectral phases of the currents dip to around 140° due to excitation of the nano-rod's resonance. Actually, if excited by an appropriate QD from topmost point, electric field resonate at this specific wavelength. The wavelength of phase dip can vary depending on the geometry of the scatterer. Changing rod length almost shifts the dip wavelength of the induced current phase; however, its lineshape remains more or less the same. This variable spectral phase is a key point in designing directive Yagi-Uda antennas.

3.4 Yagi-Uda Radiator

The simplest Yagi-Uda antenna consists of a driven element at the center enclosed by two parasitic elements in a linear array with different lengths. The current in the driven element induces a current to the parasitic elements through near-field coupling [127]. The current phase in the longest element (reflector) leads that of the driven element and prevents the power from propagation in its direction. The phase of the shortest element which is named as the director lags that of the driven element and

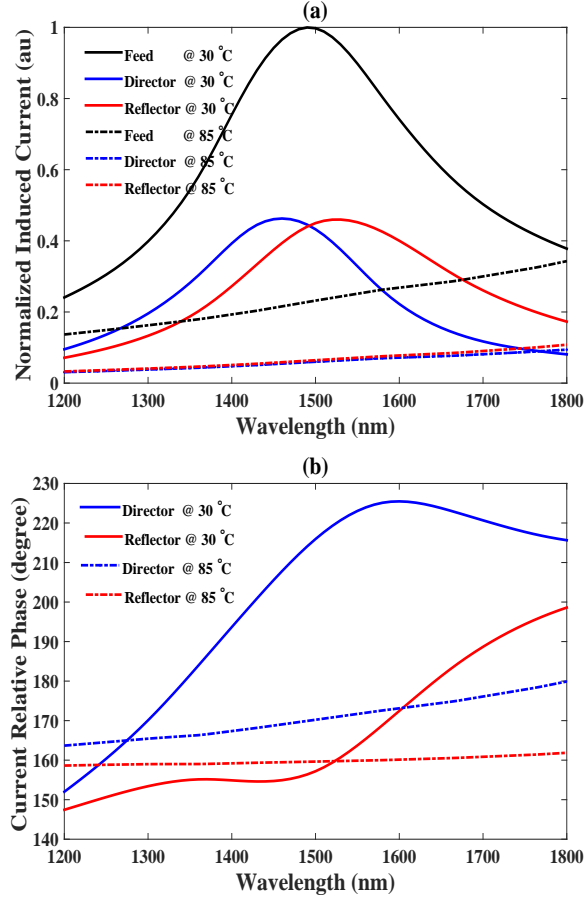


Figure 3.3: Induced current at designed Yagi-Uda elements due to QD excitation of feed element at low/high temperatures. (a) normalized amplitude and (b) phase difference of parasitic elements currents from driven feed currents.

causes radiated energy to propagate toward the director. Therefore a uniaxial directive radiation pattern can be obtained by this configuration [159]. Here an antenna is designed to assess the uniaxial directive pattern at $\lambda = 1500$ nm which can be switched by setting the temperature. Geometrical properties, material properties and excitation of the driven element are the same as the given example of Fig 3.1. The reflector is 10 % longer than the driven element and the director is 10 % shorter than it. These elements are parallel and placed 200 nm away from the feed. Hence that the bottom points are aligned rather than the centers due to imposed restriction of manufacturing techniques.

Fabrication of each golden cylinder requires a separate complete lithography assisted printing due to height difference of features.

The induced current in the driven element due to the QD source resonates at $\lambda = 1500$ nm, $T=30$ °C because it excites the first resonance mode of this element; as a result, the radiation is enhanced at this wavelength. The increment of the current also causes amplification of the induced currents in the parasitic elements. Because these elements have different resonance wavelengths, their spectral maximum takes place away from 1500 nm. The current in these elements is weaker than the feed because they are not driven directly.

The resonance of driven element at 85 °C is very weak and appears around 2000 nm (as can be seen from Fig. 3.1), here the spectral response up to 1800 nm in Fig 3.3 is presented. The induced current at the driven element is weaker at $T=85$ °C around $\lambda = 1500$ nm compared to 30 °C at this wavelength due to higher VO₂ losses at the former temperature. The induced currents in the parasitic elements are also weaker at this temperature compared to 30 °C. The coupling between the elements is affected by VO₂ loss at higher temperatures, hence the parasitic to driven current ratio is decreased from 0.44 at 30 °C to 0.28 at 85 °C.

The phase difference of the induced current in the parasitic elements compared to the driven element's current phase is demonstrated in Fig. 3.3 (b). Both elements have plane spectral phases in the range of 1200-1800 nm at $T=85$ °C; therefore both are reflectors at this temperature. The elements current phases at room temperature vary with wavelength due to resonance and inter-element effects. The current phase of one element compared to the feed is in the range of 0-180° while the current phase of the other element is in the range of 180-360° between $\lambda = 1350$ nm and 1650 nm. Since then, the radiator has a reflector and a director and so it is a Yagi-Uda antenna in this wavelength range. The current profile in parasitic elements no longer matches Fig. 3.2 due to near-field interaction of antenna elements.

The multi-reflection of wave between elements provide a feedback mechanism which imposes the lineshape of director/reflector currents. Because of this mechanism, the

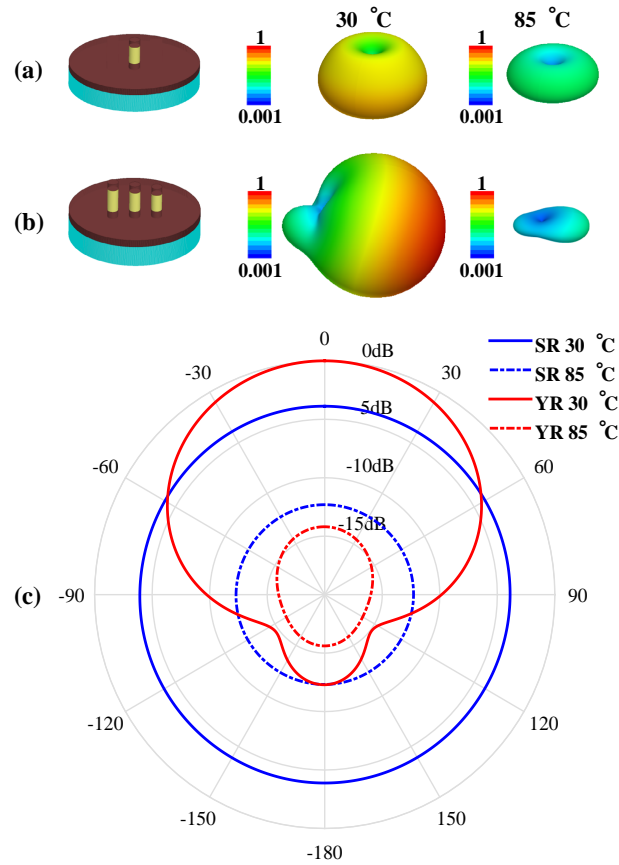


Figure 3.4: A comparison between designed single radiator and Yagi-Uda radiation patterns at low/high temperatures. (a) single radiator (SR) antenna and its patterns shown in log scale, (b) Yagi-Uda radiator (YR) and its patterns drawn in log scale, (c) Normalized antennas patterns at azimuth in dB scale.

amplitude of parasitic currents follows the variations of feed current. The phase of parasitic currents has to follow the phase variation of feed as well. Therefore it is weakly dependent to the other factors such as inter-element distances. However by increment of parasitic elements distance from the feed, the relative phase of induced current in them slightly increases. Then, by changing this distance, the relative phase shift could be tuned to lie closer to the desired values if necessary.

3.5 Discussion

By using the induced currents over the structure and substrate, the far field radiation pattern of the antenna is calculated. The radiation patterns of the single radiator (SR)

at the far field region in $T=30\text{ }^{\circ}\text{C}$ and $T=85\text{ }^{\circ}\text{C}$ are shown in Fig. 3.4 (a). In both cases the pattern is omnidirectional; however, at higher temperatures radiation is diminished due to metallic VO₂ losses. The pattern for Yagi-Uda antenna (YR) is depicted in Fig. 3.4 (b) and as expected, the directivity of the antenna is increased at $30\text{ }^{\circ}\text{C}$. The pattern's front to back ratio reaches 12 dB (power scale) at room temperature while it is less than 1.5 dB at high temperature. A comparison of the antenna's radiation at two temperatures in azimuth is exhibited in Fig. 3.4 (c). The Yagi-Uda antenna improves the radiation power manipulation and it enables directive power emission which can be switched by switching the antenna temperature.

A comparison of a single radiator to the Yagi-Uda radiator at $85\text{ }^{\circ}\text{C}$ has valuable information about the physics of the antennas. The radiation is diminished for Yagi-Uda compared to the single radiator at this temperature. Interestingly, the parasitic elements increased the loss of system and this loss increment can be explained using the current study in Fig. 3.3. The current of the parasitic elements are almost 0.28 times that of one of the driven element while their phase is almost 180° at $\lambda = 1500$ nm. Therefore, they reduce around 0.28 of the driven element electric field intensity at the far field region. Then the radiation of Yagi-Uda is weaker than that of the single radiator at high temperatures by a factor of $1 - (1 - 0.28)^2 = 0.4816$ at the far field. This point can be inferred from Fig. 3.4 (c) which shows the antenna radiation in azimuth angles. The dashed red curve which demonstrates Yagi-Uda radiation at higher temperatures is approximately 2-3 dB weaker than the dashed blue curve which represents the single radiator radiation at the higher temperature.

3.6 Conclusion

In conclusion, temperature dependent directive vertically polarized radiation was obtained by a simple optical Yagi-Uda array exposed by a thin layer of VO₂. The temperature variation switches resonance and loss rate of driven element as well as amplitude and the phase of the induced current in the parasitic elements of the antenna. Antenna

pattern variation was explained correlating these currents to Yagi-Uda performance and comparing it to the single radiator currents. It was shown that this fabricable antenna using conventional lithography techniques greatly switches the azimuth radiation rate and directionality, hence it can facilitate integrated optical communication on chips.

Chapter 4

Reflection Switching by VO₂ Phase Transition in Core-Shells

4.1 Introduction

Vanadium dioxide has been employed as a major material for thermochromic composites which temperature variation alternates the optical index in the material [161, 162] because of extreme sensitivity of spatially confined electrons in its partially filled orbitals [97]. Below a specific temperature the monoclinic structure of the material shows an insulator behavior while beyond the transition temperature it undergoes a reversible insulator to metal phase transition by changing its crystal structure. The change in the optical index of the material modulates scattering properties of the composite.

Transmittance and absorbance of VO₂-based thermochromic coatings has been investigated in the literature extensively and under different conditions [?, 163, 164] trying to keep the coating transparency in room temperature and increasing light modulation by material phase transition. However, their reflection switchability has not received a enough consideration yet. Basically VO₂ has been known as a low-reflectivity material at its bulk and thin-film formats which phase transition causes slight reflection switchability [97].

On the other hand, adding shells to the resonating nano-particles with light can

manipulate their resonance properties. As a result, the structures can assess nano-scale control of energy [165,166], enhanced light harvesting [167] and tuning localized surface plasmons [168]. VO₂ has been employed as the core for in numbers of studies [169–174]. VO₂ in VO₂@Au core-shells provide a negative light absorption feedback to self regulate temperature in a fixed range [169]. SiO₂ added to the VO₂ nano-particle to enhance VO₂ chemical stability in the thermochromic coating [173]. TiO₂ shells affect the self-cleaning of the switchable VO₂ nano-particles [172]. Furthermore, the dynamic tunability of VO₂-based core-shells has been investigated because of their luminous transmittance advantage over VO₂ thin films [171]. However, in all these studies the shell adds negligible reflectivity switching to the composites or even functions as the anti-reflective coating.

Here the controllable reflectivity of VO₂ nano-spheres and core-shells have been studied by temperature switching. It is shown that at room temperature an array of VO₂ particles may have up to 33 % reflectivity due to their resonance with incident light at the design wavelength. However, the reflectivity of particles degrade by switching the temperature to $T = 85^{\circ}C$ because of higher inherent losses of VO₂ at its metallic phase. To obtain higher reflectivity at room temperature, a spherical core-shell structure was proposed to further reduces the losses in the nano-particle while reflectivity of the structure at high temperature remains low. Using this technique up to 67% of the incident power and 95% of reflected light is shown to be dynamically controllable by switching the temperature of composite. Then th reflectance analysis of randomly distributed nano-particles illustrated these composites may have similar behavior to their regularly distributed counterpart but no their lattice resonance fades in the reflectance spectra.

4.2 Reflectivity of VO₂ Nano-sphere

Reflection from the surface of a particle array is directly related to the ability of each particle to scatter light. On the other hand, small particle with dimensions comparable

to wavelength can have remarkable scattering properties. A mathematical formulation has been developed for simple particle shapes such as spheres. This method analyzes isolated dielectric sphere by calculating the electric and magnetic resonance modes inside the particle and studies the scattering characteristics from their interference in the far-field region [175]. Hence, sub micro-meter semiconductors in the infrared regime can be modeled by their first order mode electric and magnetic polarizabilities neglecting the small contribution from higher order modes. The backscattering cross-section of the low-loss dielectric sphere normalized to its physical cross-section can be written by:

$$Q_b = 9 \frac{|a_1 - b_1|^2}{k_0^2 r^2} \quad (4.1)$$

In this equation, a_1 and b_1 are Mie scattering coefficients corresponding the transverse magnetic and transverse electric modes, k_0 is the wavenumber in ambient medium and r is the radius of particle. Supposing a high reflection control is desired around $\lambda = 2000$ nm, VO2 particle has to have a considerable back-scattering coefficient at the lower temperature in this wavelength. In the high temperature, it is expected that the inherent VO2 losses decrease the backscattering and shrink the reflection. To obtain an optimum particle size for higher backscattering, Eq. (4.1) is utilized here. The host material is a polymer with dispersion-less index of 1.5 and VO2 index is $3.2 + 0.17j$ at $\lambda = 2000$ nm. Extracting the scattering coefficients from [46] and applying it to Eq. (4.1) for various r gives an overview of the Q_b dependence to particle radius. Fig. 4.1 (a) illustrate this dependency for a range of radius r . Hence this equation is not valid for metallic VO2 nano-particles due to higher losses of VO2 at high temperatures starting from $T = 30$ °C.

This figure shows that for small radius, Q_b is very small. Basically when the particle size is much smaller than the wavelength, back-scattering cross-section of the particle is a negligible fraction of its physical cross-section. However, for insulator VO2 this function increases smoothly up to 64 % of the physical cross-section around $r = 320$ nm, then decreases till $r = 400$ nm. Q_b goes greater than 0.64 for larger particle

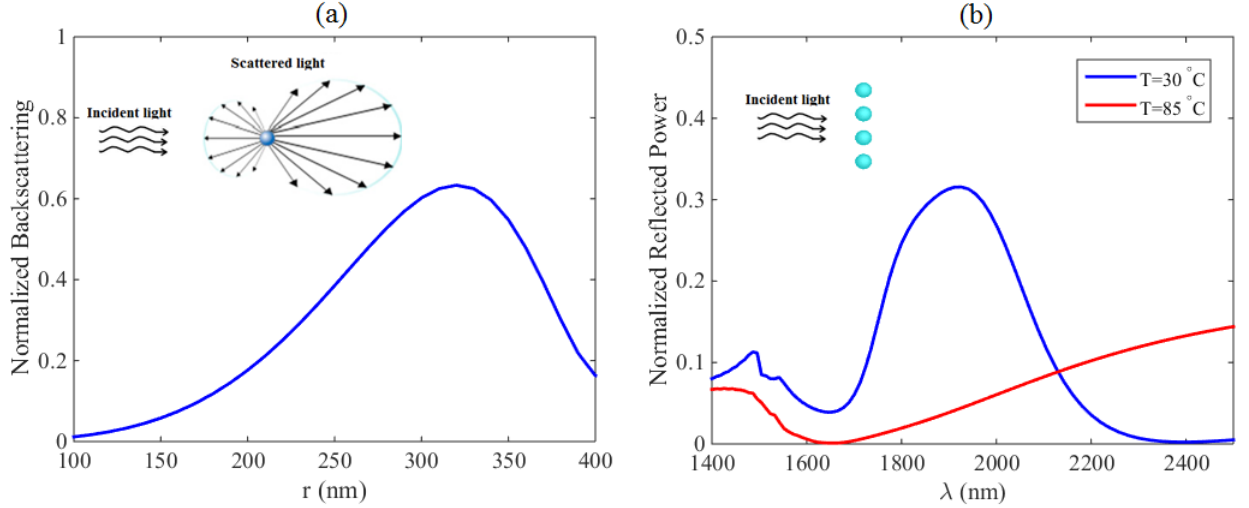


Figure 4.1: (a) Normalized back-scattering cross-section of insulator VO2 at $\lambda = 2000$ nm as a function of particle radius. (b) Power reflection by a 2-D array of VO2 spheres with $r = 320$ nm and lattice period of $a = 1000$ nm upon normal incident of light at mid-infrared wavelengths. Increasing ambient temperature from $T = 30^\circ\text{C}$ to $T = 85^\circ\text{C}$ changes the optical index of VO2, consequently, the reflectivity of the array switches.

sizes but after the first local minimum at $r = 400$ nm the higher order modes become significant which we are not interested in. Therefore, a particle of $r = 320$ nm can give the maximum backward scattering.

After obtaining the optimum particle size for higher back-scattering at $\lambda = 2000$ nm, the reflection from its 2-dimensional array is examined here. Array lattice (a) is selected so that the particle covers a considerable physical cross-section of the array. Consequently, a cannot be quite larger than the particle diameter. Here it is assumed that $a = 1000$ nm, as a result the particle takes 32% of the array surface. This array has been analyzed numerically using a commercial-grade simulator [176] based on the finite-difference time-domain (FDTD) method [177]. The dispersive optical index of VO2 at is taken from [97] and silicon optical index is extracted from the experiment data by Palik [108]. To avoid the optical index hysteresis of VO2 which takes place between $T = 50^\circ\text{C}$ and $T = 80^\circ\text{C}$ [97], $T = 30^\circ\text{C}$ and $T = 85^\circ\text{C}$ are selected for this examination. However, for the temperatures between these two states, the optical property of VO2 smoothly varies between the moderate loss insulator state at $T = 30^\circ\text{C}$ to the lossy metallic state at $T = 85^\circ\text{C}$. Hence the reflection at every wavelength

smoothly changes between the curves in Fig. 4.1 (b).

Fig. 4.1 (b) shows that by shifting temperature from $T = 30\text{ }^{\circ}\text{C}$ to $T = 85\text{ }^{\circ}\text{C}$, the reflectivity of the array changes due to insulator to metal phase change in VO₂. The difference of reflectivity at two temperatures maximizes around $\lambda = 1900\text{ nm}$ which the insulator VO₂ particle resonates by the incident wave. At this wavelength, VO₂ phase transition switches the reflectivity from 0.33 to 0.05. For longer wavelength starting from $\lambda = 2140\text{ nm}$ reflectivity of metallic VO₂ at $T = 85\text{ }^{\circ}\text{C}$ exceeds the reflectivity of insulator VO₂ at $T = 30\text{ }^{\circ}\text{C}$. Fundamentally, the phase transition of VO₂ changes the resonance of the particle as well as its loss factor. At metallic phase the particle resonate at longer wavelengths with relatively higher absorption rate. Therefore, the reflectivity of metallic VO₂ particles at these wavelength can be grater than their insulator state which does not experience a considerable resonance. However, due to higher losses, the reflectivity switching cannot reach 25 % of the incident power at $\lambda = 1900\text{ nm}$. This amount is comparable with the reported thermal reflectivity controls in literature [178].

It is noteworthy that the resonance of reflection at $T = 30\text{ }^{\circ}\text{C}$ has slightly shifted from the designed wavelength. Basically, this shift takes place because of the resonance mode interactions in closely packed coupled particles. The maximum reflection wavelength can be set to the designed value by tuning (in this case increasing) the radius of particle.

4.3 Reflectivity of VO₂@Si Core-shells

The temperature switching of VO₂ manipulates up to 25 % of the incident power in the described structure. This performance is good; however, higher switching capability is desirable for power-handling and sensing applications. Decreasing the lattice size can increase the reflected power at the low-loss resonances. Nonetheless, controlling inter-particle distance at realization of the structure is a difficult task. Here an alternative method based on spherical core-shell structures is employed. In this technique, a lower-loss material is utilized as the shell of VO₂ spherical core to diminish the absorbed

power in the structure at resonances. To avoid resonance shifts, silicon which has a close optical index to insulator VO2 is selected for shell. Keeping the outer radius of the structure constant and increasing the thickness of shell, the effect of low-loss shell can be studied on the ability of structure to control the power reflectivity. Fig. 4.3 illustrate the power reflectivity for different shell thicknesses at $T = 30\text{ }^{\circ}\text{C}$ and $T = 85\text{ }^{\circ}\text{C}$. The optical properties of Si are taken from [108].

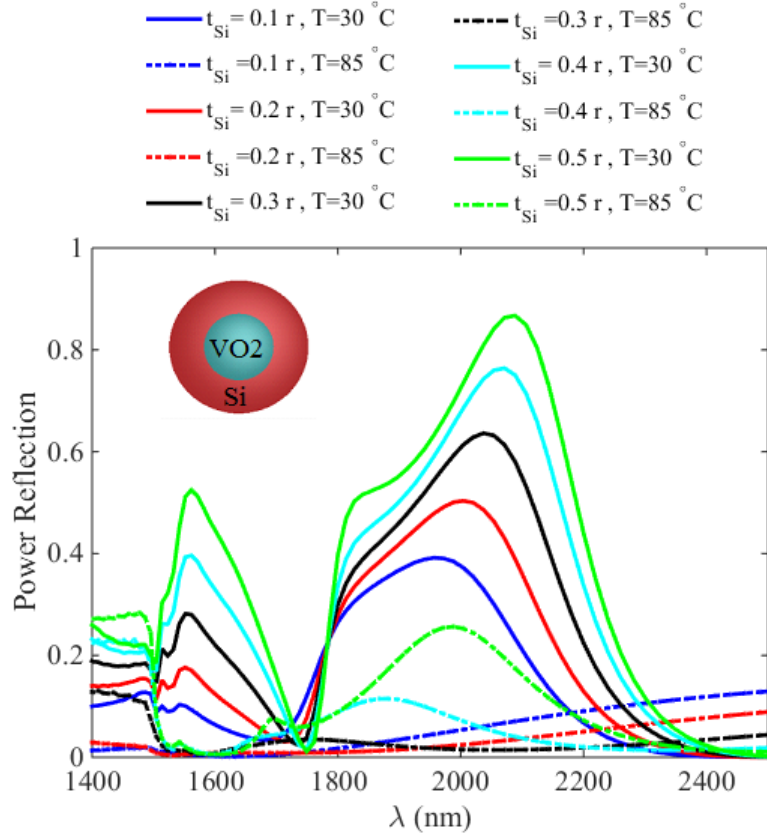


Figure 4.2: Power reflection by a 2-D array of VO2@Si core-shells with $r = 320\text{ nm}$ and lattice period of $a = 1000\text{ nm}$ upon normal incident of light at mid-infrared wavelengths for $T = 30\text{ }^{\circ}\text{C}$ to $T = 85\text{ }^{\circ}\text{C}$ and different Si thicknesses.

Fig. 4.2 clearly shows the reflectivity of core-shell is increased by increment of silicon thickness at room temperature. Although the overall diameter of the core-shell remains constant the peak of reflectivity response tends to lower wavelength as the shell thickness grows. Index of silicon which is slightly bigger than the index of VO2 at $T = 30\text{ }^{\circ}\text{C}$ causes this shift. At $T = 30\text{ }^{\circ}\text{C}$ by increasing the thickness of Si shell

up to $t_{Si} = 0.4r$, the reflectivity of the core-shell array decreases. By further increasing the shell thickness, the structure resonates around $\lambda = 2000$ nm at high temperature. This resonance raises because the metallic VO2 losses diminishes as the volume of VO2 decreases in the structure, as a result the reflectivity around the resonance increases. Therefore, the difference between power reflectivity at $T = 30$ °C and $T = 85$ °C maximizes at $t_{Si} = 0.4r$. The maximum power reflection controllability core-shells reaches 70 % of the incident wave which is quite bigger than the VO2 spheres of the same size and to best of author's knowledge it is twice the best reflectivity control by VO2 phase transition reported in the literature [179].

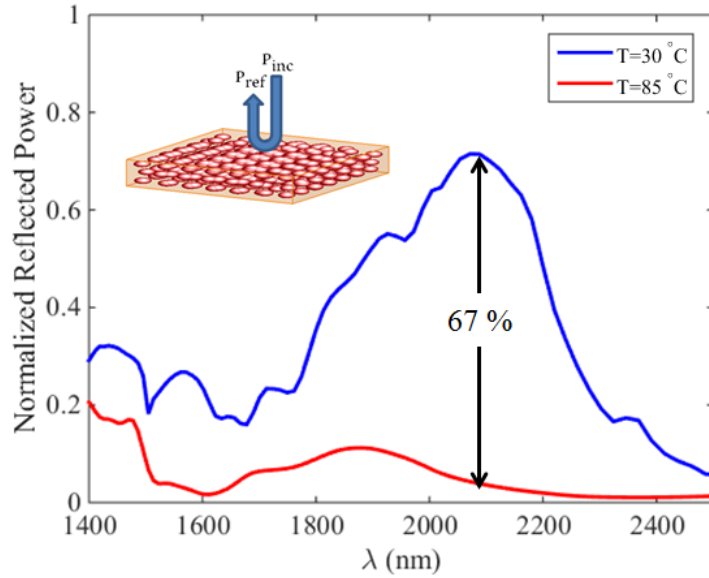


Figure 4.3: Power reflectivity by a 3-D array of randomly distributed VO2@Si core-shells at $T = 30$ °C and $T = 85$ °C. The nano-particles radius is 320 nm and Si has 30 % of the overall thickness.

In reality having an array with precise lattice is difficult and implementation of such an structure is expensive. Rather than that, composites which the same core-shell sizes but with random distribution over space is much affordable. Here core-shells are randomly relocated in a 3 layer array of VO2@Si to study the effect of irregular composites. The random distances have the Gaussian distribution with standard deviation of 170 nm which is almost 50 % of the nano-particle radius. The numerical analysis here is limited to a $3 \times 3 \times 3$ array with random relocations. The reflectivity of this

composite in $T = 30\text{ }^{\circ}\text{C}$ and $T = 85\text{ }^{\circ}\text{C}$ is shown in Fig. 3.

Fig. 3 depicts the ability of a randomly distributed VO₂@Si core-shells to manipulate the reflected power by shifting the temperature. Although for the certain case which is analyzed here the reflectivity has some deviation from the curve of Fig. 2 (b) for the same Si thickness, the overall trend of both curve matches neglecting the surface resonance around $\lambda = 1600\text{ nm}$. It can be concluded that this resonance is not an inherent resonance of the core-shell but it comes from the regular lattice of the structure in Fig. 2 (b). By fading the lattice, this resonance fades too. If standard deviation of the nano-particle distribution further increases, the reflection curve for limited number of them may have more fluctuation than Fig. 4.3. It is expected that the spectral response gets smoother as area of the structure expanded. However, proving this matter requires higher computational capacity which is not available yet. We can expect the randomly distributed core-shells of Si@VO₂ switch the reflection up to 67 % by temperature switching in the structure.

4.4 Conclusion

In summary the insulator to metal phase change of vanadium dioxide was employed to control the reflection spectrum from spherical Si@VO₂ core-shells embedded in a polymer host material. Reflectivity performance of these nano-particles was studied for deterministic and randomly distributed particles. The core-shells could switch the reflection up to 67 % in power scale by temperature switching in the structure from $T = 30\text{ }^{\circ}\text{C}$ to $T = 85\text{ }^{\circ}\text{C}$.

Chapter 5

Chimera States in Optical Nano-resonators

5.1 Introduction

Identical coupled oscillators were expected to either synchronize in phase or drift incoherently indefinitely; however, it has been shown that this conventional wisdom is not accurate enough where the coupling is nonlocal i.e. the coupling strength decays with distance between the oscillators [180]. Kuramoto demonstrated that even for identical oscillators, which are similarly coupled, the long-last coexistence of synchronous and incoherent oscillations is possible. Later it was shown that the coexistence can be stable when the number of the oscillators tends to infinity [181]. Nowadays, these symmetry broken spatio-temporal oscillation patterns are known as chimera states due to their similarity to mythological Greek dragons with incongruous heads [182].

The states were shown to exist for various coupling mechanisms both in pure mathematical systems [182–186] or physical frameworks [187–190]. Recently, the numerical demonstration was extended by designing appropriate experiments to show the chimeras in mechanical systems [191, 192]. In optical regime, chimeras happen among semiconductor laser oscillators [193, 194]. Even though the concept have been recently demonstrated, researchers have already found interesting applications for them ranging

from brain electrical activity modeling [195] to electrical power grid analysis [196]. The applications spectrum is going to be extended as the states are proven to exist in new physical phenomena [197].

Concurrently, surface plasmons paved the way for amplification of stimulated emission in nano-scale optics recently [198]. Spasers as tiny brothers of lasers generate or amplify coherent localized optical fields in a surface plasmon cavity [199,200]. Although the ultrafast behavior of isolated spasers is studied in the literature, their performance in arrays worth attention particularly because of their application periodic structure of lossy meta-materials [201–203].

Here, the chimera states for an array of nano-optical oscillators was demonstrated, the oscillators are devised based on spasers scheme. Each oscillator consists of a plasmonic dimer cavity, which exchange optical energy with an active medium located at the dimer hot-spot. The cavity is modified so that the surface plasmon trap ultra-short and intense optical pulses at the active medium for long-last amplitude mediated oscillation. The dimers are locally coupled by their near-field region neighbors and the coupling strength decreases by distance. It is shown that for the eight-identical oscillator system, which are placed symmetrically over the perimeter of a circle, concurrent coherent and incoherent behavior is observed among the array members. While the oscillator of each group seems to be locked together, one member can scape from synchronization for a while and return to coherency again or it can orchestrate with the other groups. The effect of coupling strength on the phase scape pace is studied for this system using FDTD numerical analysis. Strong coupling can force the array members to fully synchronize while weaker coupling demonstrate chimera states in the array of oscillators.

5.2 Oscillator Design

Here an optical nano-oscillator is devised based on a nonlinear active material which receives feedback from a plasmonic resonator. A plasmonic dimer provides a cavity

with a high quality factor at the gap, assuming the gap is filled by a material which a fraction of its atoms have active 4-level 2 electron atomic system. Normally, the valence electrons of the active atoms or molecules occupy two lower energy levels, E_0 and E_1 . Since two free electrons of each active molecule cannot occupy the same energy levels, the population of these levels, are almost equal. On the other hand due to small probability of electron transition to higher energy levels, there is a small population of electrons in E_2 and E_3 . Applying a short electric field pulse with appropriate frequency and polarization pumps the electrons of E_0/E_1 to E_3/E_2 ; the electron store this energy while they are in E_3 and E_2 .

A nano-plasmonic dimer helps this energy to be released in a quite slower pace and provide the required energy for long last oscillations. The dimer which is shown in Fig. 1 (a) consists of two identical metallic cylinders placed coaxially with a small gap in between filled with a semiconductor active characteristics. An external electric field with a polarization parallel to the dimer axis excites dipoles in each cylinder which confines the electric field around their poles. Because two dipole are coaxially adjacent, their bright mode can be stimulated to intensify the electric field confinement [204,205]. The dimer resonance is set to $f_{30} = (E_3 - E_0)/h$ where h is Planck's constant. After the excitation, distorted electron population tends to occupy lower energy levels. Hence, the pumped electrons to E_3 mostly move to E_2 and level E_0 becomes fully populated by the electron transitions from E_1 while electron transitions between E_3-E_0 and E_2-E_1 are relatively slower. Here the pump intensity and duration is set so that electron population inversion between E_0 and E_2 does not happen and the system remains in thermal equilibrium. Based on Fermi-Dirak relation below [206], a very small portion of E_2 population remains in or moves to E_3 .

$$\langle \frac{N_i}{N_j} \rangle = \frac{1}{\alpha e^{(E_i - E_j)/kT} + 1} \quad (5.1)$$

In equation (5.1) $\langle \rangle$ indicates average for the variable inside, $N_{i/j}$ shows the population in level i/j , α is a constant which depends to the source of valence electrons (*e.g.* $\alpha = 0.5$ for donor impurities in semiconductors), k is Boltzman constant and T

is temperature in Kelvin scale. An oscillating field in the high quality factor resonator can excite electrons of E_3 to move back to ground state (E_0) and release their energy by radiation. At the same time N_2 refills lost electrons of N_3 and this process continues to settlement of electric field inside the resonator. However, since the radiated energy of the electrons is coherent to the resonator field, it compensate a portion of lost energy in the resonator. Consequently, electric field of frequency f_{30} last longer time in the resonator.

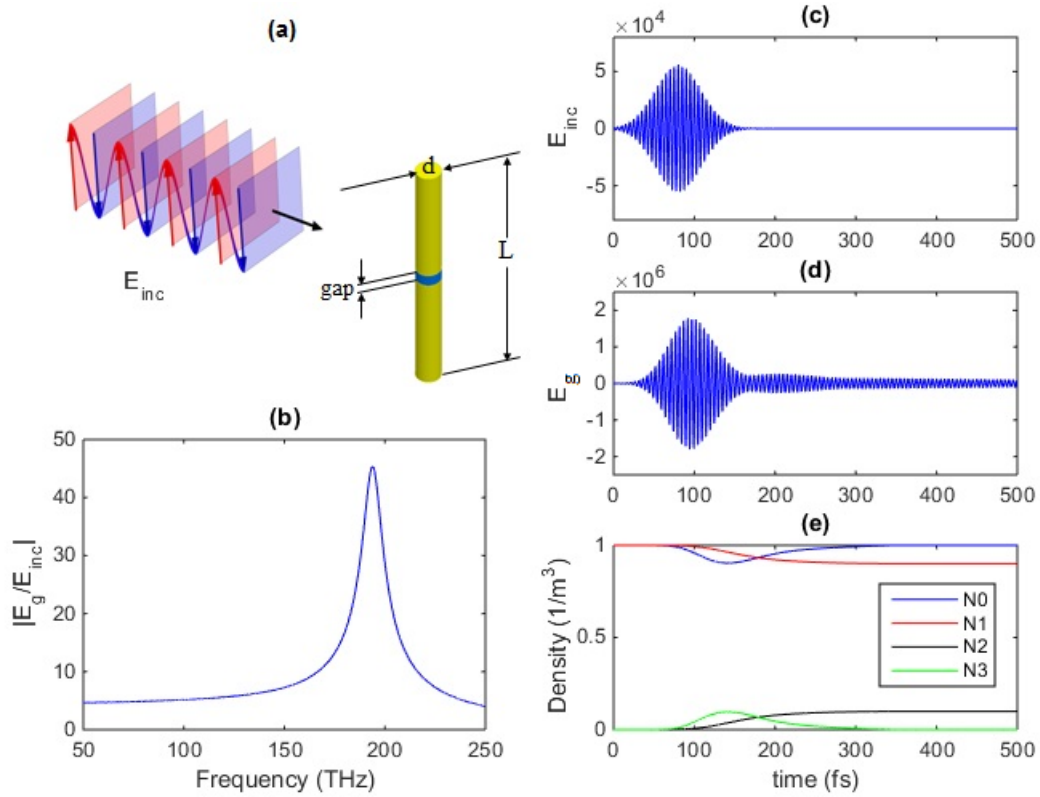


Figure 5.1: Plasmonic nano-oscillator (a) Geometry and excitation illustration. (b) Electric field enhancement of the plasmonic dimer at the center of its gap before doping InP. (c) Time-profile of the electric field excitation. (d) Probed electric field at the dimer gap. (e) Electron population density normalized to the density of active molecules in InP at the center of the plasmonic dimer.

A FDTD-based commercial solver of Maxwell's equations is employed to analyze this model numerically. The dimer materials and dimensions are as follow: Cylinders metal has Drude properties of gold [207] with plasma frequency of 2068 THz and damping constant of 1 THz. The length of each cylinder is 135 nm and the thickness is 20 nm;

the gap between them is 20 nm filled with Indium phosphate (InP) with optical index extracted from experiment [108]. This structure is embedded in glass with dispersionless optical index of 1.5. The intrinsic electric field enhancement of plasmonic dimer in the gap center point is shown at Fig. 5.1 (b) in before InP doping by impurity. The maximum quality factor of the resonator is around 18 which shows that the dissipated power of the resonator in each cycle of incident wave is a decent fraction of the oscillating energy inside it.

InP is doped with an impurity so that it has valence electrons density of $2 \times 10^{22} m^{-3}$ with $(E_3 - E_0)/h = 200$ THz and $(E_2 - E_1)/h = 100$ THz. Damping coefficient for E_3-E_0 and E_2-E_1 transitions is 1 THz and decay time for both is 0.3 ns. The non-radiating transition between E_3-E_2 and E_1-E_0 takes places with pretty faster decay lifetime of 0.1 ps. The performance of described nano-oscillator when it is excited by a plane wave with a Gaussian temporal profile is shown in Fig. 5.1 (c-e); the excitation pulse amplitude is 5.6×10^5 V/m, the half-power span of the pulse is 40 fs and the modulation frequency is f_{30} .

As Fig. 5.1 (d) suggests, after the excitation pulse disappears, electric field inside the cavity oscillates with a relatively smaller amplitude but for a longer time. Since the cavity is lossy, the oscillation cannot last for such a long time in absence of the active medium. However, the active material absorbs the pump energy and release it with slower pace to drive this long-last oscillation inside the cavity. Fig. 2 (e) shows the electron population density of each level over time normalized by the population density of the active molecules doped to InP. After the pulse disappears a majority of pumped electrons to E_3 settle in E_2 . The cavity damps electron transition from E_2 to E_1 due to its low quality factor at f_{21} . Nonetheless, the cavity has a good quality factor at f_{30} and based on Eq 5.1 there is a small population of electrons in this energy level. As a result, any electric field of frequency f_{30} inside the resonator cavity may cause E_3 electrons to release a photon at f_{30} and move to E_0 . The photons compensate a portion of lost energy in the resonator, therefore the quality of plasmon oscillation increases. However, this energy is not strong enough to overcome the loss and cause

lasing. Consequently, the amplitude of the oscillation decreases and so the amount of released photons which depend on the intensity of the electric field inside the material decreases over the course of time. Thus this system can be considered as an amplitude mediated nano-optical oscillator [208].

5.3 Chimera States Demonstration

Here an array of identical oscillators are used to demonstrate the chimera states in a nano-resonator array system. Therefore, concurrent incoherent and coherent oscillation among the identical oscillators was illustrated. An eight element symmetric array is formed by using the oscillators discussed in the previous section. The dimers are arranged vertically over the perimeter of a horizontal circle 45° apart from each other, forming an the eight element symmetric array. A schematic illustration of the array is demonstrated in Fig. 3.3 (a). Due to the symmetry of the system, all the members have identical coupling to the rest of array and one may expect their inherent resonance frequency is exactly identical.

The active medium is stimulated initially to push the electrons in the active medium to higher energy levels. The higher levels electron populations of all the oscillators can be kept identical by exciting the array with a cylindrically symmetric waves. Initial oscillations caused by the pump settles down over the course of time. It is assumed that the array ended up with the following normalized population densities in the active medium: $N_0 \approx 1$, $N_2 \approx 0.9$, $N_2 \approx 0.1$ and $N_3 \approx 0$. Illuminating this array by additional plane wave pulse with Gaussian temporal profile causes long-last oscillation inside the array. This oscillation can be coherent among the array member depending on their coupling strength. As an example the temporal response of this array to a pulse with amplitude of 1V/m , span of 40 fs and modulation by 100 THz is depicted in Fig. 3.3 when the array radius $r = 27.5\text{ nm}$.

Fig. 5.2 (b) depicts the probed electric field at the center of oscillator 1 as an example of the array reaction to the incident pulse turbulence. Since the oscillators

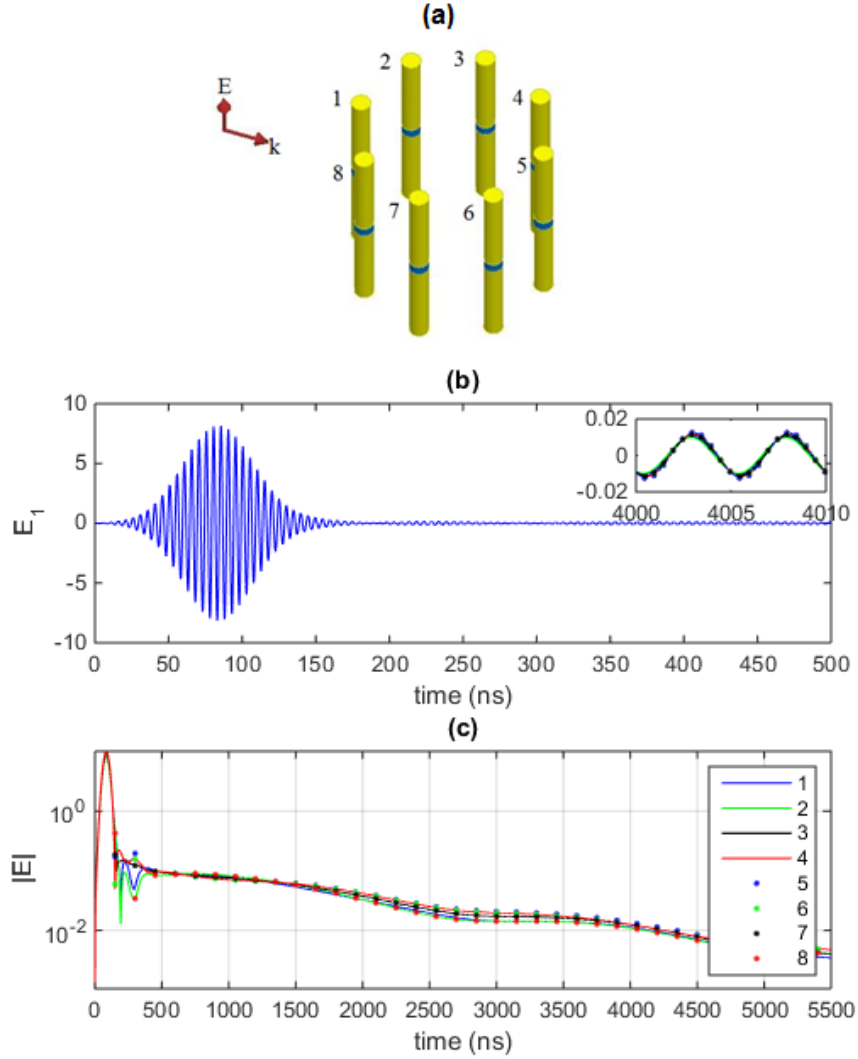


Figure 5.2: An example of full coherency in the oscillator array: (a) Geometry of the array, (b) Probed electric field at the center of oscillator 1, (c) The amplitude of oscillations

are located very closed to each other ($r = 27.5$ nm), their coupling is strong enough to force all the oscillators synchronize. The inset figure shows the oscillation after 4000 ns. Apparently, all the oscillator have equal amplitude and negligible phase difference. The amplitudes change over time is shown in figure 5.2 (c). Right after applying the pulse there are transient responses in the array which disappear over time. As the transient response diminishes, the oscillations amplitude decreases smoothly. In this step, the oscillation amplitude of the members barely degrade from the average of the array. In order to compare the oscillations, the phase of electric field at the probe is sampled by

the following equation:

$$\phi_n = \angle E(n\Delta t) - 2\pi f_{30} \cdot n\Delta t \quad (5.2)$$

The sampled phase of oscillators at Fig. 5.2 alongside with the sampled phase of similar geometries with $r = 35$ nm, $r = 70$ nm and $r = 140$ nm are plotted in Fig. 3.4. It is noteworthy that the amplitude variation of the oscillators over time is smooth and resembles those of Fig. 5.2 (c).

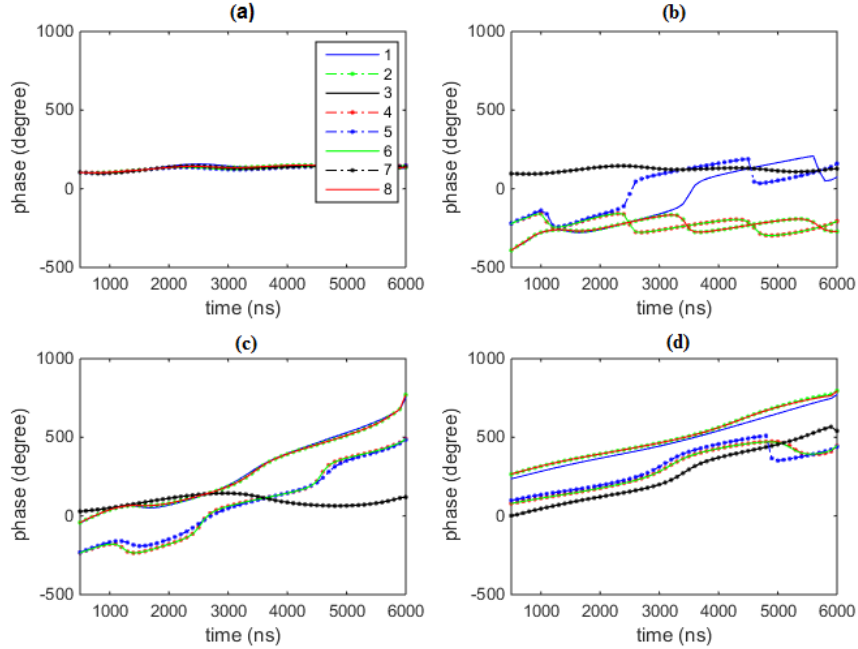


Figure 5.3: Sampled phase of the oscillators electric field at their gap for different array geometries: (a) $r = 27.5$ nm, (b) $r = 35$ nm, (c) $r = 70$ nm and (d) $r = 140$ nm.

Fig. 5.3 (a) illustrate the coherency of oscillators for $r = 27.5$ nm case because all the oscillations over time keep a common phase and stick to that. The sampled phase at this figure shows if a slight change in phase happens, all the oscillators follow that change and stay synchronized. As the distance (d) between the oscillators increases, the coupling decreases by $1/d^{3/2}$ [209] because the dimer dimensions are comparable to the distance to the neighbor dimers. In this condition, the inter-particle coupling is governed mainly by Coulombic forces between the localized surface plasmons. For $r = 35$ nm the coupling is strong enough to tie some of the oscillators in coherency. Due

to symmetry of geometry and excitation, members 3 and 7 of the array are synchronized together. That means the oscillators phase difference does not change over a period of time which is quite larger than the oscillation period. The other array members are synchronized together for numbers of time intervals. Between these intervals one or two oscillators escape from synchronization and oscillate incoherently. However, they synchronize again after almost 180 degrees of phase change and remain coherent for a longer time. This pattern repeats over time almost every 1000 ns. The array at current form is divided to two synchronized populations that are incoherent together, therefore this state is an indication of the chimera oscillations in this nano-particle system.

As the distance between the oscillators further increases, their coupling further reduces. For $r = 70\text{nm}$ case (Fig. 5.3 (c)), synchronization is weaker and the array becomes a 3 head chimera due to three distinct phase patterns among the oscillators. Interestingly, two groups of closed neighbors stay synchronized and any escape by a member is compensated by the other members in the group to keep synchronization. For instance, oscillators 4 and 6 escape from a common head with 5, but 5 tracks their changes in $t = 1200\text{ fs}$ and $t = 4800\text{ ns}$. However, for $r = 70\text{ nm}$ the phase escapes by the oscillators are smaller compared to them for $r = 35\text{ nm}$. As a result the coupling strength directly affects the chimera head number and the strength of phase escape from synchronization. Fig. 4 (d) shows the array for $r=140\text{nm}$, in this case the coupling is weak so that oscillators seemed to oscillate freely. As a result their sampled phase diagram is smoother. Some members are synchronized and keep track phase escapes of the other members from their chimera head. If the coupling among the members become negligible for very long distances they oscillate freely but coherently. However, this coherency is more sensitive to noise compared to the coherency of strongly coupled oscillators. By comparing these 4 cases it can be concluded that synchronization tendency among the oscillator decreases by increasing their distance. The chimera states merge where the coupling between the oscillators are big enough to keep some of the oscillator coherent but not strong enough to force all of them to synchronize together.

5.4 Method

The atoms with 4-level 2 electron atomic system is modeled as follows. Each two interacting electrons in the active molecule occupy quantized energy levels; the electrons can absorb/radiate emission with certain frequencies and move between these energy levels. A simplified model of such active medium is shown in Fig. 5.4.

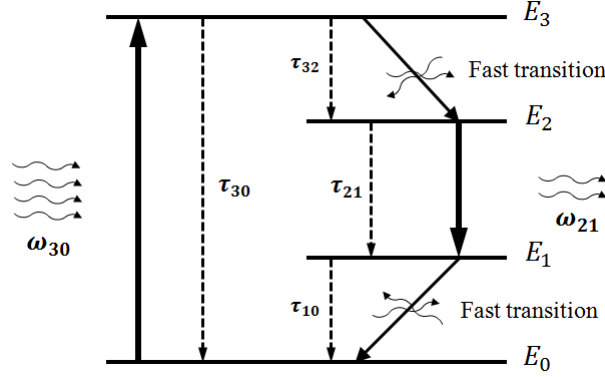


Figure 5.4: Simplified model of electron interaction with photons in an active medium with 2 electron 4 energy level atomic system.

Electron transitions between E_3 and E_2 take place in a quite fast pace and the accompanied emissions have random phases. As a result, the average radiation of electron transition between these two energy levels becomes zero as the number of transitions increases. Electron transition between E_1 and E_0 has a similar treatment. However, E_0 - E_3 and E_2 - E_1 transitions are relatively slower and the resulted emissions can be coherent to an imposed electromagnetic wave. The electron interaction with the wave obeys Bloch relation which results in the following governing equation for the polarization density in the medium [210]:

$$\frac{d^2 P_{21}}{dt^2} + \gamma_{21} \frac{dP_{21}}{dt} + \omega_{21}^2 P_{21} = \zeta_{21}(N_2 - N_1)E \quad (5.3)$$

$$\frac{d^2 P_{30}}{dt^2} + \gamma_{30} \frac{dP_{30}}{dt} + \omega_{30}^2 P_{30} = \zeta_{30}(N_3 - N_0)E \quad (5.4)$$

P_{ij} is the polarization density between level i and level j , γ_{ij} , ω_{ij} and ζ_{ij} are the corresponding deshaping factor and angular frequency and electron density adjustment

factor. N_k is the electron population density in energy levels k , E is the electric field. The electron population density in each level changes over time because of non-radiative decays and radiative emissions. The population density is governed by the Pauli Exclusion Principle and coupled electron density rate equation which are presented below:

$$\frac{dN_3}{dt} = -\frac{N_3(1-N_2)}{\tau_{32}} - \frac{N_3(1-N_0)}{\tau_{30}} + \frac{1}{h\omega_{30}}E \cdot \frac{dP_{30}}{dt} \quad (5.5)$$

$$\frac{dN_2}{dt} = \frac{N_3(1-N_2)}{\tau_{32}} - \frac{N_2(1-N_1)}{\tau_{21}} + \frac{1}{h\omega_{21}}E \cdot \frac{dP_{21}}{dt} \quad (5.6)$$

$$\frac{dN_1}{dt} = \frac{N_2(1-N_1)}{\tau_{21}} - \frac{N_1(1-N_0)}{\tau_{10}} - \frac{1}{h\omega_{21}}E \cdot \frac{dP_{21}}{dt} \quad (5.7)$$

$$\frac{dN_0}{dt} = \frac{N_3(1-N_0)}{\tau_{30}} + \frac{N_1(1-N_0)}{\tau_{10}} - \frac{1}{h\omega_{30}}E \cdot \frac{dP_{30}}{dt} \quad (5.8)$$

In this set of equations, τ_{ij} is the electron average decay time between levels i and j ; h is Plank's constant. The electron population densities vary with radiative emission $E \cdot dP_{ij}/dt$ and non-radiative emission decay term $(N_i - N_j)/\tau_{ij}$.

The Maxwell equations in FDTD method are implemented by discretization of the problem in time and space. A backward difference formula was used to implement time derivatives of the fields and a central difference formula was employed for space domain derivatives. The optical index of dispersive medium was converted or approximated to a sum of complex-conjugate pole-residue pairs and conventional FDTD method was modified for those mediums.

5.5 Conclusion

In summary, the chimera states for optical nano-resonators was demonstrated. A surface plasmon based nano-optical oscillator was modeled using numerical implementation of Maxwell's equations coupled with the electron rate equations of the active medium located in the plasmon hot-spot. It was shown that the oscillator has a stable oscillation phase and amplitude over time. Chimera states were demonstrated and studied using this oscillator system in an eight element array of closely and symmetri-

cally coupled oscillators. It was found that the synchronization and the rate of escape from synchronization depends on the distance of the oscillators from each other. The chimera heads merge when the coupling between the oscillators are big enough to keep some of the oscillator coherent but not strong enough to force all of them synchronize together.

Chapter 6

Conclusion and Future Works

6.1 Conclusions

In this study it is shown employing VO₂ in plasmonic structures empower them to respond to light dynamically. The scattering properties of localized surface plasmon in presence of this material were studied for different applications.

In the first application, a compact and ultrathin plasmonic metasurface was proposed for an ultra-short pulse shaping in the optical regime. A planar array of nanoplasmonic particles was employed to manipulate the transmission spectrum of propagating ultra-short pulses to shape its temporal characteristics. The method was able to broaden, compress and reshape the polarization of ultrashort pulses with great control over its characteristics by engineering the resonances of the ultrathin plasmonic metasurface. A reconfigurable localized surface plasmon band-stop optical filter driven by insulator to metal phase transition of vanadium dioxide was proposed based on the performance of the devised metasurface. A Joule heating mechanism that is transparent for the polarization of input pulse was designed to control the thermal phase transition of the material. The resulting permittivity variation of vanadium dioxide tailors spectral response of the transmitted pulse from the stack. Depending on factors such as the position and width of the spectrum of the input pulse with respect to the resonance of the band-stop filter, the thin film stack can compress/expand the output pulse span

up to 20% or shift its phase up to 360 degree. To provide further functionality to the optical filter, stacked filters were suggested to improve the expansion rates up to 90 %. Furthermore, it was demonstrated that the proposed optical filter can compensate input carrier frequency shifts and pulse span variations to preserve the output pulse shape.

In the second application a temperature driven switchable-beam vertically polarized directional antenna for micro/nano scale optical communications was proposed and studied. Temperature-enabled phase transitions of a thin layer of vanadium dioxide reshaped the beam of a Yagi-Uda antenna by changing the directionality of the radiation pattern and altering the emission rate. The role of each antenna element in the Yagi-Uda array's emission was demonstrated at different temperatures by comparing the amplitudes and phases of induced currents in the elements. Thus a substantial directional gain switching was shown using resonance damping manipulation of antenna elements.

In the third application, the metal to insulator phase change of VO₂ was employed to control the reflection spectrum from spherical core-shells embedded in a polymer host material. Reflectivity performance of these nano-particles was studied for deterministic and randomly distributed particles in space. The highly reflective core-shells were devised at near-infrared regime based on the Mie scattering formulation and it was shown that up to 67 % of the incident power can be controlled by manipulation of temperature in the structure.

Finally, the chimera states for optical nanoresonators were studied and demonstrated. The oscillators were designed based on a plasmonic dimer cavity, which interchanges radiative energy with an active medium located at its hot-spot. Therefore, they formed an amplitude mediated oscillating system. Finite-difference time-domain (FDTD) based numerical analysis of a circular array of the coupled oscillators revealed that regardless of identical nature, treatment was not concordant over time. The effect of coupling strength on the phase scape/synchronization of the oscillators was investigated for the optical nanoresonator system. It was shown that for the eight-identical

oscillator system, which are placed symmetrically over the perimeter of a circle, the array can be divided to several subgroups of concurrent coherent and incoherent members. While the oscillator of each subgroup seemed to be locked together, one member could scape from synchronization for a while and return to coherency again or it could sync with the other groups. The effect of coupling strength on the phase scape pace was studied for this system using FDTD numerical analysis. Strong coupling could force the array members to fully synchronize while weaker coupling demonstrated chimera states in the array.

6.2 Suggestions for Future Works

Based on the achievements of this thesis the following headlines are suggested for further extending the work:

- Dynamic polarization shaping can be achieved based on the devised method in Section 2.4. The thermally controllable phase transition of VO₂ can be employed by a multi-resonance surface plasmon to show and assess versatile polarization manipulation.
- Ultra-fast behavior of the Yagi-Uda antenna for on-chip application can be investigated. The current study assumes the power dissipation inside the antenna structure is not changing the phase of VO₂ but in high power communication, the power level may reach a threshold which degrade the functionality of antenna thermal control. The calculation of this threshold worth of attention as well as the work extension for multi-director Yagi-Uda. The effect of extra directors on the directionality of the antenna in presence of VO₂ is a fascinating item that can be studied. Also horizontally polarized Yagi-Udas which have horizontal resonating elements can be functionalized by VO₂ phase transition and their controllability by temperature variation can be studied.
- The core-shells studied in this work for controlling light reflection are spherical.

The same survey can be repeated for cylindrical Mie scatterer or for a different set of materials for the host and shell.

- The chimera states in different set of oscillators with larger or smaller population can be investigated. Different array shapes and arrangement can be studied. As an example chimera states in the rectangular or cubic lattices worth of attention due to their similarity to metamaterial lattices where the amplifiers-oscillators are employed to reduce the propagation loss. Chimera states sensitivity to external distortion and noise can be studied too.

Bibliography

- [1] Katherine A Willets and Richard P Van Duyne. Localized surface plasmon resonance spectroscopy and sensing. *Annu. Rev. Phys. Chem.*, 58:267–297, 2007.
- [2] Stefan Alexander Maier. *Plasmonics: fundamentals and applications*. Springer Science & Business Media, 2007.
- [3] Mark W Knight, Heidar Sobhani, Peter Nordlander, and Naomi J Halas. Photodetection with active optical antennas. *Science*, 332(6030):702–704, 2011.
- [4] Wei Li and Jason Valentine. Metamaterial perfect absorber based hot electron photodetection. *Nano Lett.*, 14(6):3510–3514, 2014.
- [5] Anthony J Morfa, Kathy L Rowlen, Thomas H Reilly III, Manuel J Romero, and Jao van de Lagemaat. Plasmon-enhanced solar energy conversion in organic bulk heterojunction photovoltaics. *Appl. Phys. Lett.*, 92(1):013504, 2008.
- [6] Seungchul Kim, Jonghan Jin, Young-Jin Kim, In-Yong Park, Yunseok Kim, and Seung-Woo Kim. High-harmonic generation by resonant plasmon field enhancement. *Nature*, 453(7196):757–760, 2008.
- [7] Eesa Rahimi and Kürşat Şendur. Femtosecond pulse shaping by ultrathin plasmonic metasurfaces. *JOSA B*, 33(2):A1–A7, 2016.
- [8] Darrick E Chang, Anders S Sørensen, Eugene A Demler, and Mikhail D Lukin. A single-photon transistor using nanoscale surface plasmons. *Nat. Phys.*, 3(11):807–812, 2007.
- [9] Lukas Novotny. Effective wavelength scaling for optical antennas. *Phys. Rev. Lett.*, 98(26):266802, 2007.
- [10] Antonio Bianconi, S Stizza, and R Bernardini. Critical behavior of the plasmon resonance at the metal-insulator transition in $v o 2$. *Phys. Rev. B*, 24(8):4406, 1981.
- [11] Imogen M Pryce, Koray Aydin, Yousif A Kelaita, Ryan M Briggs, and Harry A Atwater. Highly strained compliant optical metamaterials with large frequency tunability. *Nano Lett.*, 10(10):4222–4227, 2010.

- [12] Fumin Huang and Jeremy J Baumberg. Actively tuned plasmons on elastomerically driven au nanoparticle dimers. *Nano Lett.*, 10(5):1787–1792, 2010.
- [13] Jun-Yu Ou, Eric Plum, Liudi Jiang, and Nikolay I Zheludev. Reconfigurable photonic metamaterials. *Nano Lett.*, 11(5):2142–2144, 2011.
- [14] Shamashis Sengupta, Kevin Wang, Kai Liu, Ajay K Bhat, Sajal Dhara, Junqiao Wu, and Mandar M Deshmukh. Field-effect modulation of conductance in vo2 nanobeam transistors with hfo2 as the gate dielectric. *Appl. Phys. Lett.*, 99(6):062114, 2011.
- [15] Nikhil Shukla, Arun V Thathachary, Ashish Agrawal, Hanjong Paik, Ahmedullah Aziz, Darrell G Schlom, Sumeet Kumar Gupta, Roman Engel-Herbert, and Suman Datta. A steep-slope transistor based on abrupt electronic phase transition. *Nat. Commun.*, 6:7812, 2015.
- [16] Philippe Ben-Abdallah and Svend-Age Biehs. Phase-change radiative thermal diode. *Appl. Phys. Lett.*, 103(19):191907, 2013.
- [17] Yue Yang, Soumyadipta Basu, and Liping Wang. Radiation-based near-field thermal rectification with phase transition materials. *Appl. Phys. Lett.*, 103(16):163101, 2013.
- [18] PJ Van Zwol, Karl Joulain, Philippe Ben-Abdallah, and Joël Chevrier. Phonon polaritons enhance near-field thermal transfer across the phase transition of vo2. *Phys. Rev. B*, 84(16):161413, 2011.
- [19] Philippe Ben-Abdallah and Svend-Age Biehs. Near-field thermal transistor. *Phys. Rev. Lett.*, 112(4):044301, 2014.
- [20] Hasan Kocer, Serkan Butun, Edgar Palacios, Zizhuo Liu, Sefaattin Tongay, Deyi Fu, Kevin Wang, Junqiao Wu, and Koray Aydin. Intensity tunable infrared broadband absorbers based on vo2 phase transition using planar layered thin films. *Sci. Rep.*, 5, 2015.
- [21] Sébastien Cueff, Dongfang Li, You Zhou, Franklin J Wong, Jonathan A Kurvits, Shriram Ramanathan, and Rashid Zia. Dynamic control of light emission faster than the lifetime limit using vo2 phase-change. *Nat. Commun.*, 6:8636, 2015.
- [22] Peiman Hosseini, C David Wright, and Harish Bhaskaran. An optoelectronic framework enabled by low-dimensional phase-change films. *Nature*, 511(7508):206–211, 2014.
- [23] Mikhail A Kats, Deepika Sharma, Jiao Lin, Patrice Genevet, Romain Blanchard, Zheng Yang, M Mumtaz Qazilbash, DN Basov, Shriram Ramanathan, and Federico Capasso. Ultra-thin perfect absorber employing a tunable phase change material. *Appl. Phys. Lett.*, 101(22):221101, 2012.

- [24] Hao Wang, Yue Yang, and Liping Wang. Wavelength-tunable infrared metamaterial by tailoring magnetic resonance condition with vo2 phase transition. *J. Appl. Phys.*, 116(12):123503, 2014.
- [25] Tun Cao, Chen-wei Wei, Robert E Simpson, Lei Zhang, and Martin J Cryan. Broadband polarization-independent perfect absorber using a phase-change metamaterial at visible frequencies. *Sci. Rep.*, 4, 2014.
- [26] Mikhail A Kats, Romain Blanchard, Patrice Genevet, Zheng Yang, M Mumtaz Qazilbash, DN Basov, Shriram Ramanathan, and Federico Capasso. Thermal tuning of mid-infrared plasmonic antenna arrays using a phase change material. *Opt. Lett.*, 38(3):368–370, 2013.
- [27] ZL Samson, KF MacDonald, F De Angelis, Behrad Gholipour, K Knight, CC Huang, E Di Fabrizio, DW Hewak, and NI Zheludev. Metamaterial electro-optic switch of nanoscale thickness. *Appl. Phys. Lett*, 96(14):143105, 2010.
- [28] Matthew J Dicken, Koray Aydin, Imogen M Pryce, Luke A Sweatlock, Elizabeth M Boyd, Sameer Walavalkar, James Ma, and Harry A Atwater. Frequency tunable near-infrared metamaterials based on vo 2 phase transition. *Opt. Express*, 17(20):18330–18339, 2009.
- [29] Tom Driscoll, S Palit, Mumtaz M Qazilbash, Markus Brehm, Fritz Keilmann, Byung-Gyu Chae, Sun-Jin Yun, Hyun-Tak Kim, SY Cho, N Marie Jokerst, et al. Dynamic tuning of an infrared hybrid-metamaterial resonance using vanadium dioxide. *Appl. Phys. Lett*, 93(2):024101, 2008.
- [30] MD Goldflam, Tom Driscoll, Brian Chapler, Omar Khatib, N Marie Jokerst, Sabarni Palit, DR Smith, Bong-Jun Kim, Giwan Seo, Hyun-Tak Kim, et al. Reconfigurable gradient index using vo2 memory metamaterials. *Appl. Phys. Lett*, 99(4):044103, 2011.
- [31] Mengkun Liu, Harold Y Hwang, Hu Tao, Andrew C Strikwerda, Kebin Fan, George R Keiser, Aaron J Sternbach, Kevin G West, Salinporn Kittiwatanakul, Jiwei Lu, et al. Terahertz-field-induced insulator-to-metal transition in vanadium dioxide metamaterial. *Nature*, 487(7407):345–348, 2012.
- [32] DW Ferrara, ER MacQuarrie, J Nag, AB Kaye, and RF Haglund Jr. Plasmon-enhanced low-intensity laser switching of gold:: vanadium dioxide nanocomposites. *Appl. Phys. Lett.*, 98(24):241112, 2011.
- [33] JY Suh, EU Donev, DW Ferrara, KA Tetz, LC Feldman, and RF Haglund Jr. Modulation of the gold particle–plasmon resonance by the metal–semiconductor transition of vanadium dioxide. *J. Optics A*, 10(5):055202, 2008.

- [34] Tun Cao, Chenwei Wei, and Libang Mao. Numerical study of achiral phase-change metamaterials for ultrafast tuning of giant circular conversion dichroism. *Sci. Rep.*, 5, 2015.
- [35] Xinghui Yin, Martin Schaferling, Ann-Katrin U Michel, Andreas Tittl, Matthias Wuttig, Thomas Taubner, and Harald Giessen. Active chiral plasmonics. *Nano Lett.*, 15(7):4255–4260, 2015.
- [36] Jonghwan Kim, Hyungmok Son, David J Cho, Baisong Geng, Will Regan, Sufei Shi, Kwanpyo Kim, Alex Zettl, Yuen-Ron Shen, and Feng Wang. Electrical control of optical plasmon resonance with graphene. *Nano Lett.*, 12(11):5598–5602, 2012.
- [37] Gang Chen, Yong Wang, Miaoxin Yang, Jun Xu, Sook Jin Goh, Ming Pan, and Hongyu Chen. Measuring ensemble-averaged surface-enhanced raman scattering in the hotspots of colloidal nanoparticle dimers and trimers. *J. ACS*, 132(11):3644–3645, 2010.
- [38] Bartłomiej Grześkiewicz, Krzysztof Ptaszyński, and Michał Kotkowiak. Near and far-field properties of nanoprisms with rounded edges. *Plasmonics*, 9(3):607, 2014.
- [39] Jian Ye and Pol Van Dorpe. Plasmonic behaviors of gold dimers perturbed by a single nanoparticle in the gap. *Nanoscale*, 4(22):7205–7211, 2012.
- [40] RE Noskov, AE Krasnok, and Yu S Kivshar. Nonlinear metal–dielectric nanoantennas for light switching and routing. *New J. Phys.*, 14(9):093005, 2012.
- [41] NS Lapshina, RE Noskov, and Yu S Kivshar. Nonlinear nanoantenna with self-tunable scattering pattern. *JETP Lett.*, 96(12):759–764, 2013.
- [42] Xiaoyan YZ Xiong, Li Jun Jiang, Wei EI Sha, Yat Hei Lo, and Weng Cho Chew. Compact nonlinear yagi-uda nanoantennas. *Sci. Rep.*, 6, 2016.
- [43] Ivan S Maksymov, Andrey E Miroshnichenko, and Yuri S Kivshar. Actively tunable bistable optical yagi-uda nanoantenna. *Opt. Express*, 20(8):8929–8938, 2012.
- [44] Yan Lu, Yu Mei, Markus Drechsler, and Matthias Ballauff. Thermosensitive core–shell particles as carriers for ag nanoparticles: modulating the catalytic activity by a phase transition in networks. *Angew. Chem. Int. Ed.*, 45(5):813–816, 2006.
- [45] Shuyi Li. *VO₂-based thermochromic and nanothermochromic materials for energy-efficient windows: Computational and experimental studies*. PhD thesis, Acta Universitatis Upsaliensis, 2013.

- [46] Christian Mätzler. Matlab functions for mie scattering and absorption, version 2. *IAP Res. Rep.*, 8:1–24, 2002.
- [47] T Andrew Taton, Gang Lu, and Chad A Mirkin. Two-color labeling of oligonucleotide arrays via size-selective scattering of nanoparticle probes. *J. ACS*, 123(21):5164–5165, 2001.
- [48] Sarmimala Hore, Carmen Vetter, Rainer Kern, Herman Smit, and Andreas Hirsch. Influence of scattering layers on efficiency of dye-sensitized solar cells. *Sol. Energ. Mat. Sol. Cells*, 90(9):1176–1188, 2006.
- [49] P Spinelli, MA Verschuuren, and A Polman. Broadband omnidirectional antireflection coating based on subwavelength surface mie resonators. *Nat. Commun.*, 3:692, 2012.
- [50] ED Potter, JL Herek, S Pedersen, Q Liu, and AH Zewail. Femtosecond laser control of a chemical reaction. *Nature*, 355(6355):66–68, 1992.
- [51] Andreas Assion, T Baumert, M Bergt, T Brixner, B Kiefer, V Seyfried, M Strehle, and G Gerber. Control of chemical reactions by feedback-optimized phase-shaped femtosecond laser pulses. *Science*, 282(5390):919–922, 1998.
- [52] Ahmed H Zewail. Femtochemistry: Atomic-scale dynamics of the chemical bond. *J. Phys. Chem. A*, 104(24):5660–5694, 2000.
- [53] Andrew M Weiner and DE Leaird. Generation of terahertz-rate trains of femtosecond pulses by phase-only filtering. *Opt. Lett.*, 15(1):51–53, 1990.
- [54] Jiangfeng Zhu, Takashi Tanigawa, Tao Chen, Shaobo Fang, Keisaku Yamane, Taro Sekikawa, and Mikio Yamashita. Ultrabroadband spectral amplitude modulation using a liquid crystal spatial light modulator with ultraviolet-to-near-infrared bandwidth. *Appl. Opt.*, 49(3):350–357, 2010.
- [55] Andrew M Weiner. Ultrafast optical pulse shaping: A tutorial review. *Opt. Commun.*, 284(15):3669–3692, 2011.
- [56] Sonia Boscolo and Christophe Finot. Nonlinear pulse shaping in fibres for pulse generation and optical processing. *Intl J. Optics*, 2012, 2012.
- [57] Leonid Glebov, Vadim Smirnov, Eugeniu Rotari, Ion Cohanoschi, Larissa Glebova, Oleg Smolski, Julien Lumeau, Christopher Lantigua, and Alexei Glebov. Volume-chirped bragg gratings: monolithic components for stretching and compression of ultrashort laser pulses. *Opt. Eng.*, 53(5):051514–051514, 2014.
- [58] Periklis Petropoulos, Morten Ibsen, AD Ellis, and David J Richardson. Rectangular pulse generation based on pulse reshaping using a superstructured fiber bragg grating. *J. Lightwave Technol.*, 19(5):746, 2001.

- [59] Jian-Qiang Liu, Ling-Ling Wang, Meng-Dong He, Wei-Qing Huang, Dianyuan Wang, BS Zou, and Shuangchun Wen. A wide bandgap plasmonic bragg reflector. *Opt. Express*, 16(7):4888–4894, 2008.
- [60] Dmitrii Yu Stepanov and Leonardo Corena. Bragg grating fabrication with wide range coarse and fine wavelength control. *Opt. Express*, 22(22):27309–27320, 2014.
- [61] Vikrant Chauhan Kumar Chauhan. Pulse compression and dispersion control in ultrafast optics. 2011.
- [62] Monika Pawłowska, Alexander Patas, Georg Achazi, and Albrecht Lindinger. Parametrically shaped femtosecond pulses in the nonlinear regime obtained by reverse propagation in an optical fiber. *Opt. Lett.*, 37(13):2709–2711, 2012.
- [63] Nils Krebs, Igor Pugliesi, and Eberhard Riedle. Pulse compression of ultrashort uv pulses by self-phase modulation in bulk material. *Appl. Sci.*, 3(1):153–167, 2013.
- [64] Mark I Stockman, Sergey V Faleev, and David J Bergman. Coherent control of femtosecond energy localization in nanosystems. *Phys. Rev. Lett.*, 88(6):067402, 2002.
- [65] Mark I Stockman, David J Bergman, and Takayoshi Kobayashi. Coherent control of nanoscale localization of ultrafast optical excitation in nanosystems. *Phys. Rev. B*, 69(5):054202, 2004.
- [66] Martin Aeschlimann, Michael Bauer, Daniela Bayer, Tobias Brixner, F Javier Garcia de Abajo, Walter Pfeiffer, Martin Rohmer, Christian Spindler, and Felix Steeb. Adaptive subwavelength control of nano-optical fields. *Nature*, 446(7133):301–304, 2007.
- [67] T Brixner, FJ García de Abajo, J Schneider, C Spindler, and Walter Pfeiffer. Ultrafast adaptive optical near-field control. *Phys. Rev. B*, 73(12):125437, 2006.
- [68] Rüştü Umut Tok and Kürşat Şendur. Femtosecond pulse shaping using plasmonic snowflake nanoantennas. *Phys. Rev. A*, 84(3):033847, 2011.
- [69] Fadi I Baida. Spatiotemporal sub-wavelength near-field light localization. *Opt. Express*, 18(14):14812–14819, 2010.
- [70] Sarah L Stebbings, Frederik Süßmann, Ying Ying Yang, A Scrinzi, Maxim Durach, Anastasia Rusina, Mark I Stockman, and Matthias F Kling. Generation of isolated attosecond extreme ultraviolet pulses employing nanoplasmonic field enhancement: optimization of coupled ellipsoids. *New J. Phys.*, 13(7):073010, 2011.

- [71] Martin Aeschlimann, Michael Bauer, Daniela Bayer, Tobias Brixner, Stefan Cunovic, Frank Dimler, Alexander Fischer, Walter Pfeiffer, Martin Rohmer, Christian Schneider, et al. Spatiotemporal control of nanooptical excitations. *Proc. Natl Aca. Sci.*, 107(12):5329–5333, 2010.
- [72] Richard V Andaloro, Henry J Simon, and Robert T Deck. Temporal pulse reshaping with surface waves. *Appl. Opt.*, 33(27):6340–6347, 1994.
- [73] PP Vabishchevich, A Yu Frolov, MR Shcherbakov, AA Grunin, TV Dolgova, and AA Fedyanin. Magnetic field-controlled femtosecond pulse shaping by magneto-plasmonic crystals. *J. Appl. Phys.*, 113(17):17A947, 2013.
- [74] PP Vabishchevich, MR Shcherbakov, VO Bessonov, TV Dolgova, and AA Fedyanin. Femtosecond pulse shaping with plasmonic crystals. *Pisma v ZhETF*, 101(11-12):885, 2015.
- [75] MR Shcherbakov, PP Vabishchevich, VV Komarova, TV Dolgova, VI Panov, VV Moshchalkov, and AA Fedyanin. Ultrafast polarization shaping with fano plasmonic crystals. *Phys. Rev. Lett.*, 108(25):253903, 2012.
- [76] Brian Ashall, José Francisco López-Barberá, Éadaoin McClean-Iltén, and Dominic Zerulla. Highly efficient broadband ultrafast plasmonics. *Opt. Express*, 21(22):27383–27391, 2013.
- [77] Zsolt L Sámson, Peter Horak, Kevin F MacDonald, and Nikolay I Zheludev. Femtosecond surface plasmon pulse propagation. *Opt. Lett.*, 36(2):250–252, 2011.
- [78] A Dechant and AY Elezzabi. Femtosecond optical pulse propagation in subwavelength metallic slits. *Appl. Phys. Lett.*, 84(23):4678–4680, 2004.
- [79] José Dintinger, Aloyse Degiron, and Thomas W Ebbesen. Enhanced light transmission through subwavelength holes. *MRS Bull.*, 30(05):381–384, 2005.
- [80] C Ropers, G Stibenz, G Steinmeyer, R Müller, DJ Park, KG Lee, JE Kihm, J Kim, QH Park, DS Kim, et al. Ultrafast dynamics of surface plasmon polaritons in plasmonic metamaterials. *Appl. Phys. B*, 84(1-2):183–189, 2006.
- [81] Francisco J Garcia-Vidal, Luis Martin-Moreno, TW Ebbesen, and L Kuipers. Light passing through subwavelength apertures. *Rev. Modern Phys.*, 82(1):729, 2010.
- [82] Rui Qiang, Ji Chen, Tianxiao Zhao, Shumin Wang, Paul Ruchhoeft, and Marilyn Morgan. Modelling of infrared bandpass filters using three-dimensional fdtd method. *Electronics Lett.*, 41(16):914–915, 2005.

- [83] Ahmadrza Hajiaboli, Mojtaba Kahrizi, and Vo-Van Truong. Optical behaviour of thick gold and silver films with periodic circular nanohole arrays. *J. Phys. D*, 45(48):485105, 2012.
- [84] Vladimir M Shalaev, Wenshan Cai, Uday K Chettiar, Hsiao-Kuan Yuan, Andrey K Sarychev, Vladimir P Drachev, and Alexander V Kildishev. Negative index of refraction in optical metamaterials. *Opt. Lett.*, 30(24):3356–3358, 2005.
- [85] Gunnar Dolling, Christian Enkrich, Martin Wegener, Costas M Soukoulis, and Stefan Linden. Simultaneous negative phase and group velocity of light in a metamaterial. *Science*, 312(5775):892–894, 2006.
- [86] Vladimir M Shalaev. Optical negative-index metamaterials. *Nat. Photon.*, 1(1):41–48, 2007.
- [87] S Pillai, KR Catchpole, T Trupke, and MA Green. Surface plasmon enhanced silicon solar cells. *J. Appl. Phys.*, 101(9):093105, 2007.
- [88] Keisuke Nakayama, Katsuaki Tanabe, and Harry A Atwater. Plasmonic nanoparticle enhanced light absorption in gaas solar cells. *Appl. Phys. Lett*, 93(12):121904, 2008.
- [89] Y Zhao, MA Belkin, and A Alù. Twisted optical metamaterials for planarized ultrathin broadband circular polarizers. *Nat. Commun.*, 3:870, 2012.
- [90] Nanfang Yu, Francesco Aieta, Patrice Genevet, Mikhail A Kats, Zeno Gaburro, and Federico Capasso. A broadband, background-free quarter-wave plate based on plasmonic metasurfaces. *Nano Lett.*, 12(12):6328–6333, 2012.
- [91] Richa Mittal, Rachel Glenn, Ilyas Saytashev, Vadim V Lozovoy, and Marcos Dantus. Femtosecond nanoplasmonic dephasing of individual silver nanoparticles and small clusters. *J. Phys. Chem. Lett.*, 6(9):1638–1644, 2015.
- [92] Qing HuoáLiu et al. Manipulating light absorption of graphene using plasmonic nanoparticles. *Nanoscale*, 5(17):7785–7789, 2013.
- [93] A Zylbersztejn and Nevill Francis Mott. Metal-insulator transition in vanadium dioxide. *Phys. Rev. B*, 11(11):4383, 1975.
- [94] Michael F Becker, A Bruce Buckman, Rodger M Walser, Thierry Lépine, Patrick Georges, and Alain Brun. Femtosecond laser excitation of the semiconductor-metal phase transition in vo2. *Appl. Phys. Lett.*, 65(12):1507–1509, 1994.
- [95] Hyun-Tak Kim, Byung-Gyu Chae, Doo-Hyeb Youn, Sung-Lyul Maeng, Gyungock Kim, Kwang-Yong Kang, and Yong-Sik Lim. Mechanism and observation of mott transition in vo2-based two-and three-terminal devices. *New J. Phys.*, 6(1):52, 2004.

- [96] Michael F Becker, A Bruce Buckman, Rodger M Walser, Thierry Lépine, Patrick Georges, and Alain Brun. Femtosecond laser excitation dynamics of the semiconductor-metal phase transition in vo2. *J. App. Phys.*, 79(5):2404–2408, 1996.
- [97] Chiranjivi Lamsal and NM Ravindra. Optical properties of vanadium oxides-an analysis. *J. Mater. Sci.*, 48(18):6341–6351, 2013.
- [98] Zachary J Thompson, Andrew Stickel, Young Gyun Jeong, Sanghoon Han, Byung Hee Son, Michael J Paul, Byounghwak Lee, Ali Mousavian, Giwan Seo, Hyun Tak Kim, Yun-Shik Lee, and Dai Sik Kim. Terahertz-triggered phase transition and hysteresis narrowing in a nanoantenna patterned vanadium dioxide film. *Nano Lett.*, 15(9):5893–5898, 2015.
- [99] Otto L Muskens, Luca Bergamini, Yudong Wang, Jeffrey M Gaskell, Nerea Zabala, CH De Groot, David W Sheel, and Javier Aizpurua. Antenna-assisted picosecond control of nanoscale phase-transition in vanadium dioxide. *Light Sci. Appl.*, pages 1–25, 2016.
- [100] Taejong Paik, Sung-Hoon Hong, E Ashley Gaulding, Humeyra Caglayan, Thomas R Gordon, Nader Engheta, Cherie R Kagan, and Christopher B Murray. Solution-processed phase-change vo2 metamaterials from colloidal vanadium oxide (vo x) nanocrystals. *ACS Nano*, 8(1):797–806, 2014.
- [101] Dang Yuan Lei, Kannatassen Appavoo, Filip Ligmajer, Yannick Sonnefraud, Richard F Haglund Jr, and Stefan A Maier. Optically-triggered nanoscale memory effect in a hybrid plasmonic-phase changing nanostructure. *ACS Photon.*, 2(9):1306–1313, 2015.
- [102] L Wang, E Radue, S Kittiwatanakul, C Clavero, J Lu, SA Wolf, I Novikova, and RA Lukaszew. Surface plasmon polaritons in vo2 thin films for tunable low-loss plasmonic applications. *Opt. Lett.*, 37(20):4335–4337, 2012.
- [103] Kelvin JA Ooi, Ping Bai, Hong Son Chu, and Lay Kee Ang. Ultracompact vanadium dioxide dual-mode plasmonic waveguide electroabsorption modulator. *Nanophotonics*, 2(1):13–19, 2013.
- [104] M Beebe, L Wang, SE Madaras, JM Klopff, Z Li, D Brantley, M Heimbürger, RA Wincheski, S Kittiwatanakul, J Lu, et al. Surface plasmon resonance modulation in nanopatterned au gratings by the insulator-metal transition in vanadium dioxide films. *Opt. Express*, 23(10):13222–13229, 2015.
- [105] N Papasimakis, YH Fu, VA Fedotov, SL Prosvirnin, DP Tsai, and NI Zheludev. Metamaterial with polarization and direction insensitive resonant transmission response mimicking electromagnetically induced transparency. *Appl. Phys. Lett.*, 94(21):211902, 2009.

- [106] Xiaopeng Shen, Yan Yang, Yuanzhang Zang, Jianqiang Gu, Jianguang Han, Weili Zhang, and Tie Jun Cui. Triple-band terahertz metamaterial absorber: Design, experiment, and physical interpretation. *Appl. Phys. Lett.*, 101(15):154102, 2012.
- [107] NI Zheludev, E Plum, and VA Fedotov. Metamaterial polarization spectral filter: Isolated transmission line at any prescribed wavelength. *Appl. Phys. Lett.*, 99(17):171915, 2011.
- [108] Edward D Palik. *Handbook of optical constants of solids*, volume 3. Academic press, 1998.
- [109] IH Malitson. Interspecimen comparison of the refractive index of fused silica*,. *J. Opt. Soc. Am.*, 55(10):1205–1209, 1965.
- [110] Antoine Monmayrant, Sébastien Weber, and Béatrice Chatel. A newcomer’s guide to ultrashort pulse shaping and characterization. *J. Phys. B*, 43(10):103001, 2010.
- [111] Cline Eypert and Mlanie Gaillet. *Optical Characterization of VO₂ Smart Materials using Spectroscopic Ellipsometry*. Horiba Scientific, 2013.
- [112] DJ Hilton, RP Prasankumar, S Fourmaux, A Cavalleri, D Brassard, MA El Khakani, JC Kieffer, AJ Taylor, and RD Averitt. Enhanced photosusceptibility near t_c for the light-induced insulator-to-metal phase transition in vanadium dioxide. *Phys. Rev. Lett.*, 99(22):226401, 2007.
- [113] Alexej Pashkin, Carl Kübler, Henri Ehrke, Ricardo Lopez, Andrej Halabica, RF Haglund Jr, Rupert Huber, and Alfred Leitenstorfer. Ultrafast insulator-metal phase transition in vo₂ studied by multiterahertz spectroscopy. *Phys. Rev. B*, 83(19):195120, 2011.
- [114] Theodore L Bergman, Frank P Incropera, David P DeWitt, and Adrienne S Lavine. *Fundamentals of heat and mass transfer*. John Wiley & Sons, 2011.
- [115] Terry M Tritt. *Thermal conductivity: theory, properties, and applications*. Springer Science & Business Media, 2005.
- [116] Raymond A Serway and John W Jewett. *Principles of physics: a calculus-based text*, volume 1. Nelson Education, 2012.
- [117] FDTD. Lumerical solutions. *Inc., Vancouver, BC, Canada*, 2003.
- [118] Vitor R Manfrinato, Lihua Zhang, Dong Su, Huigao Duan, Richard G Hobbs, Eric A Stach, and Karl K Berggren. Resolution limits of electron-beam lithography toward the atomic scale. *Nano Lett.*, 13(4):1555–1558, 2013.
- [119] Joyeeta Nag and RF Haglund Jr. Synthesis of vanadium dioxide thin films and nanoparticles. *J. Phys. Condens. Matter*, 20(26):264016, 2008.

- [120] Andrea Alù and Nader Engheta. Wireless at the nanoscale: optical interconnects using matched nanoantennas. *Phys. Rev. Lett.*, 104(21):213902, 2010.
- [121] Erik Öström, Luca Mottola, and Thiemo Voigt. Evaluation of an electronically switched directional antenna for real-world low-power wireless networks. In *Real-World Wireless Sensor Networks*, pages 113–125. Springer, 2010.
- [122] Terukazu Kosako, Yutaka Kadoya, and Holger F Hofmann. Directional control of light by a nano-optical yagi–uda antenna. *Nat. Photon.*, 4(5):312–315, 2010.
- [123] Alberto G Curto, Giorgio Volpe, Tim H Taminiau, Mark P Kreuzer, Romain Quidant, and Niek F van Hulst. Unidirectional emission of a quantum dot coupled to a nanoantenna. *Science*, 329(5994):930–933, 2010.
- [124] Toon Coenen, Ernst Jan R Vesseur, Albert Polman, and A Femius Koenderink. Directional emission from plasmonic yagi–uda antennas probed by angle-resolved cathodoluminescence spectroscopy. *Nano Lett.*, 11(9):3779–3784, 2011.
- [125] Radostin S Pavlov, Alberto G Curto, and Niek F van Hulst. Log-periodic optical antennas with broadband directivity. *Opt. Commun.*, 285(16):3334–3340, 2012.
- [126] Ivan S Maksymov, Isabelle Staude, Andrey E Miroschnichenko, and Yuri S Kivshar. Optical yagi-uda nanoantennas. *Nanophotonics*, 1(1):65–81, 2012.
- [127] Diego M Solís, José M Taboada, Fernando Obelleiro, and Luis Landesa. Optimization of an optical wireless nanolink using directive nanoantennas. *Opt. Express*, 21(2):2369–2377, 2013.
- [128] Mohsen Janipour and Farrokh Hodjat-Kashani. Directional radiation of surface plasmon polaritons at visible wavelengths through a nanohole dimer optical antenna milled in a gold film. *J. Opt. Soc. Korea*, 18(6):799–808, 2014.
- [129] Vincent KS Hsiao, Yue Bing Zheng, Bala Krishna Juluri, and Tony Jun Huang. Light-driven plasmonic switches based on au nanodisk arrays and photoresponsive liquid crystals. *Adv. Mater.*, 20(18):3528–3532, 2008.
- [130] Ragip A Pala, Ken T Shimizu, Nicholas A Melosh, and Mark L Brongersma. A nonvolatile plasmonic switch employing photochromic molecules. *Nano Lett.*, 8(5):1506–1510, 2008.
- [131] Longzhi Yang, Chongyang Pei, Ao Shen, Changyun Zhao, Yan Li, Tingge Dai, Hui Yu, Yubo Li, Xiaoqing Jiang, and Jianyi Yang. Ultracompact plasmonic switch based on graphene-silica metamaterial. *Phys. Rev. Lett.*, 104(21):211104, 2014.

- [132] Luke Sweatlock, Kenneth Diest, James Ma, Vladan Jankovic, Imogen Pryce, Ryan Briggs, and Harry Atwater. Plasmonic modulator incorporating a solid-state phase change material, June 10 2014. US Patent 8,749,866.
- [133] Yannick Salamin, Wolfgang Heni, Christian Haffner, Yuriy Fedoryshyn, Claudia Hoessbacher, Romain Bonjour, Marco Zahner, David Hillerkuss, Pascal Leuchtmann, Delwin L Elder, Larry R Dalton, Christian Hafner, and Juerg Leuthold. Direct conversion of free space millimeter waves to optical domain by plasmonic modulator antenna. *Nano Lett.*, 15(12):8342–8346, 2015.
- [134] Andrei Faraon, Charles Santori, Zhihong Huang, Kai-Mei C Fu, Victor M Acosta, David Fattal, and Raymond G Beausoleil. Quantum photonic devices in single-crystal diamond. *New J. Phys.*, 15(2):025010, 2013.
- [135] Nicholas C Harris, Davide Grassani, Angelica Simbula, Mihir Pant, Matteo Galli, Tom Baehr-Jones, Michael Hochberg, Dirk Englund, Daniele Bajoni, and Christophe Galland. Integrated source of spectrally filtered correlated photons for large-scale quantum photonic systems. *Phys. Rev. X*, 4(4):041047, 2014.
- [136] Annemarie Holleccek, Oliver Barter, Allison Rubenok, Jerome Dille, Peter BR Nisbet-Jones, Gunnar Langfahl-Klabes, Graham D Marshall, Chris Sparrow, Jeremy L OBrien, Konstantinos Poullos, et al. Quantum logic with cavity photons from single atoms. *Phys. Rev. Lett.*, 117(2):023602, 2016.
- [137] Timur Shegai, Si Chen, Vladimir D Miljković, Gülis Zengin, Peter Johansson, and Mikael Käll. A bimetallic nanoantenna for directional colour routing. *Nat. Commun.*, 2:481, 2011.
- [138] Pablo Albella, Toshihiko Shibanuma, and Stefan A Maier. Switchable directional scattering of electromagnetic radiation with subwavelength asymmetric silicon dimers. *Sci. Rep.*, 5, 2015.
- [139] Alexander Cuadrado, Francisco Javier González, and Javier Alda. Steerable optical antennas by selective heating. *Opt. Lett.*, 39(7):1957–1960, 2014.
- [140] Alexander Cuadrado, José Manuel López-Alonso, Francisco Javier González, and Javier Alda. Spectral response of metallic optical antennas driven by temperature. *Plasmonics*, pages 1–9, 2016.
- [141] Alexander V Kolobov, Paul Fons, Anatoly I Frenkel, Alexei L Ankudinov, Junji Tominaga, and Tomoya Uruga. Understanding the phase-change mechanism of rewritable optical media. *Nat. Mater.*, 3(10):703–708, 2004.
- [142] Martina Abb, Pablo Albella, Javier Aizpurua, and Otto L Muskens. All-optical control of a single plasmonic nanoantenna–ito hybrid. *Nano Lett.*, 11(6):2457–2463, 2011.

- [143] Ann-Katrin U Michel, Peter Zalden, Dmitry N Chigrin, Matthias Wuttig, Aaron M Lindenberg, and Thomas Taubner. Reversible optical switching of infrared antenna resonances with ultrathin phase-change layers using femtosecond laser pulses. *ACS Photonics*, 1(9):833–839, 2014.
- [144] Gregory Kaplan, Koray Aydin, and Jacob Scheuer. Dynamically controlled plasmonic nano-antenna phased array utilizing vanadium dioxide. *Opt. Mater. Express*, 5(11):2513–2524, 2015.
- [145] Sun-Je Kim, Kyookeun Lee, Seung-Yeol Lee, and Byoung-ho Lee. Directional switching of surface plasmon polaritons by vanadium dioxide-gold hybrid antennas. *SPIE OPTO*, pages 975621–975621, 2016.
- [146] Yuntian Chen, Peter Lodahl, and A Femius Koenderink. Dynamically reconfigurable directionality of plasmon-based single photon sources. *Phys. Rev. B*, 82(8):081402, 2010.
- [147] Wolfgang Pfaff, Arthur Vos, and Ronald Hanson. Top-down fabrication of plasmonic nanostructures for deterministic coupling to single quantum emitters. *J. Appl. Phys.*, 113(2):024310, 2013.
- [148] Constantine A Balanis. *Antenna theory: analysis and design*. John Wiley & Sons, 2016.
- [149] Yuzo Shigesato, Mikiko Enomoto, and Hidehumi Odaka. Thermo-chromic vo2 films deposited by rf magnetron sputtering using v2o3 or v2o5 targets. *Japanese J. Appl. Phys.*, 39(10R):6016, 2000.
- [150] Y Muraoka and Z Hiroi. Metal-insulator transition of vo2 thin films grown on tio2 (001) and (110) substrates. *Appl. Phys. Lett.*, 80(4):583–585, 2002.
- [151] A Zimmers, L Aigouy, M Mortier, A Sharoni, Siming Wang, KG West, JG Ramirez, and Ivan K Schuller. Role of thermal heating on the voltage induced insulator-metal transition in vo 2. *Phys. Rev. Lett.*, 110(5):056601, 2013.
- [152] Dasheng Li, Abhishek A Sharma, Darshil K Gala, Nikhil Shukla, Hanjong Paik, Suman Datta, Darrell G Schlom, James A Bain, and Marek Skowronski. Joule heating-induced metal-insulator transition in epitaxial vo2 tio2 devices. *ACS Appl. Mater. Interf.*, 8(1):12908–12914, 2016.
- [153] Peter Zijlstra et al. *Photothermal properties of gold nanorods and their application to five-dimensional optical recording*. PhD thesis, Citeseer, 2009.
- [154] RK Kramer, N Pholchai, VJ Sorger, TJ Yim, R Oulton, and X Zhang. Positioning of quantum dots on metallic nanostructures. *Nanotechnology*, 21(14):145307, 2010.

- [155] Uday K Chettiar and Nader Engheta. Modeling vanadium dioxide phase transition due to continuous-wave optical signals. *Opt. Express*, 23(1):445–451, 2015.
- [156] Ansys. v15. *HFSS ANSYS Corporation Software, Pittsburgh, PA, USA*, 15, 2014.
- [157] Tim H Taminiou, Fernando D Stefani, and Niek F van Hulst. Enhanced directional excitation and emission of single emitters by a nano-optical yagi-uda antenna. *Opt. Express*, 16(14):10858–10866, 2008.
- [158] Timur Shegai, Vladimir D Miljkovic, Kui Bao, Hongxing Xu, Peter Nordlander, Peter Johansson, and Mikael Kall. Unidirectional broadband light emission from supported plasmonic nanowires. *Nano Lett.*, 11(2):706–711, 2011.
- [159] Thomas A Milligan. *Modern antenna design*. John Wiley & Sons, 2005.
- [160] Robert L Olmon and Markus B Raschke. Antenna-load interactions at optical frequencies: impedance matching to quantum systems. *Nanotechnology*, 23(44):444001, 2012.
- [161] Jae Yong Suh, Rene Lopez, Leonard C Feldman, and RF Haglund Jr. Semiconductor to metal phase transition in the nucleation and growth of VO_2 nanoparticles and thin films. *J. Appl. Phys.*, 96(2):1209–1213, 2004.
- [162] Kinson C Kam and Anthony K Cheetham. Thermochromic VO_2 nanorods and other vanadium oxides nanostructures. *Mater. Res. Bull.*, 41(5):1015–1021, 2006.
- [163] Sihai Chen, Hong Ma, Xinjian Yi, Tao Xiong, Hongcheng Wang, and Caijun Ke. Smart VO_2 thin film for protection of sensitive infrared detectors from strong laser radiation. *Sens. Actuators A Phys.*, 115(1):28–31, 2004.
- [164] Jiadong Zhou, Yanfeng Gao, Zongtao Zhang, Hongjie Luo, Chuanxiang Cao, Zhang Chen, Lei Dai, and Xinling Liu. VO_2 thermochromic smart window for energy savings and generation. *Sci. Rep.*, 3, 2013.
- [165] Xiaoqing Huang, Shaoheng Tang, Biju Liu, Bin Ren, and Nanfeng Zheng. Enhancing the photothermal stability of plasmonic metal nanoplates by a core-shell architecture. *Adv. Mater.*, 23(30):3420–3425, 2011.
- [166] Carly S Levin, Cristina Hofmann, Tamer A Ali, Anna T Kelly, Emilia Morosan, Peter Nordlander, Kenton H Whitmire, and Naomi J Halas. Magnetic-plasmonic core-shell nanoparticles. *ACS Nano*, 3(6):1379–1388, 2009.
- [167] Michael D Brown, Teeraporn Suteewong, R Sai Santosh Kumar, Valerio DInnocenzo, Annamaria Petrosza, Michael M Lee, Ulrich Wiesner, and Henry J Snaith. Plasmonic dye-sensitized solar cells using core-shell metal-insulator nanoparticles. *Nano Lett.*, 11(2):438–445, 2010.

- [168] Chad P Byers, Hui Zhang, Dayne F Swearer, Mustafa Yorulmaz, Benjamin S Hoener, Da Huang, Anneli Hoggard, Wei-Shun Chang, Paul Mulvaney, Emilie Ringe, et al. From tunable core-shell nanoparticles to plasmonic drawbridges: Active control of nanoparticle optical properties. *Sci. Adv.*, 1(11):e1500988, 2015.
- [169] MB Cortie, A Dowd, N Harris, and MJ Ford. Core-shell nanoparticles with self-regulating plasmonic functionality. *Phys. Rev. B*, 75(11):113405, 2007.
- [170] Vilas G Pol, Swati V Pol, Jose M Calderon-Moreno, and A Gedanken. Core-shell vanadium oxide- carbon nanoparticles: Synthesis, characterization, and luminescence properties. *J. Phys. Chem. C*, 113(24):10500–10504, 2009.
- [171] S-Y Li, Gunnar A Niklasson, and Claes-Göran Granqvist. Nanothermochromics with vo₂-based core-shell structures: Calculated luminous and solar optical properties. *J. Appl. Phys.*, 109(11):113515, 2011.
- [172] Yamei Li, Shidong Ji, Yanfeng Gao, Hongjie Luo, and Minoru Kanehira. Core-shell vo₂@ tio₂ nanorods that combine thermochromic and photocatalytic properties for application as energy-saving smart coatings. *Sci. Rep.*, 3, 2013.
- [173] Yanfeng Gao, Shaobo Wang, Hongjie Luo, Lei Dai, Chuanxiang Cao, Yiliao Liu, Zhang Chen, and Minoru Kanehira. Enhanced chemical stability of vo₂ nanoparticles by the formation of sio₂/vo₂ core/shell structures and the application to transparent and flexible vo₂-based composite foils with excellent thermochromic properties for solar heat control. *Energy Environ. Sci.*, 5(3):6104–6110, 2012.
- [174] Wei Cheng, Guobo Zeng, and Markus Niederberger. Design of vanadium oxide core-shell nanoplatelets for lithium ion storage. *J. Mater. Chem. A*, 3(6):2861–2868, 2015.
- [175] Roxana Rezvani Naraghi, Sergey Sukhov, and Aristide Dogariu. Directional control of scattering by all-dielectric core-shell spheres. *Optics Lett.*, 40(4):585–588, 2015.
- [176] FDTD Solutions. Lumerical solutions, inc., vancouver, british columbia, canada, 2015.
- [177] Allen Taflove and Susan C Hagness. *Computational electrodynamics: the finite-difference time-domain method*. Artech house, 2005.
- [178] Qiang Li, Desong Fan, and Yimin Xuan. Thermal radiative properties of plasma sprayed thermochromic coating. *J. Alloys Compd.*, 583:516–522, 2014.
- [179] Shaotang Li, Yamei Li, Kun Qian, Shidong Ji, Hongjie Luo, Yanfeng Gao, and Ping Jin. Functional fiber mats with tunable diffuse reflectance composed of electrospun vo₂/pvp composite fibers. *Appl. Mater. Interf.*, 6(1):9–13, 2013.

- [180] Yoshiaki Kuramoto and Dorjsuren Battogtokh. Coexistence of coherence and incoherence in nonlocally coupled phase oscillators. *ArXiv Cond. Matt*, 2002.
- [181] Oleh E Omel'chenko. Coherence–incoherence patterns in a ring of non-locally coupled phase oscillators. *Nonlinearity*, 26(9):2469, 2013.
- [182] Daniel M Abrams and Steven H Strogatz. Chimera states for coupled oscillators. *Phys. Rev Lett.*, 93(17):174102, 2004.
- [183] Gautam C Sethia, Abhijit Sen, and Fatihcan M Atay. Clustered chimera states in delay-coupled oscillator systems. *Phys. Rev. Lett.*, 100(14):144102, 2008.
- [184] E Omelchenko, Yuri L Maistrenko, and Peter A Tass. Chimera states: The natural link between coherence and incoherence. *Phys. Rev. Lett.*, 100(4):044105, 2008.
- [185] Iryna Omelchenko, Yuri Maistrenko, Philipp Hövel, and Eckehard Schöll. Loss of coherence in dynamical networks: spatial chaos and chimera states. *Phys. Rev. Lett.*, 106(23):234102, 2011.
- [186] Simbarashe Nkomo, Mark R Tinsley, and Kenneth Showalter. Chimera states in populations of nonlocally coupled chemical oscillators. *Phys. Rev. Lett.*, 110(24):244102, 2013.
- [187] Matthias Wolfrum and E Omelchenko. Chimera states are chaotic transients. *Phys. Rev. E*, 84(1):015201, 2011.
- [188] Aaron M Hagerstrom, Thomas E Murphy, Rajarshi Roy, Philipp Hövel, Iryna Omelchenko, and Eckehard Schöll. Experimental observation of chimeras in coupled-map lattices. *Nat. Phys.*, 8(9):658–661, 2012.
- [189] Mark R Tinsley, Simbarashe Nkomo, and Kenneth Showalter. Chimera and phase-cluster states in populations of coupled chemical oscillators. *Nat. Phys.*, 8(9):662–665, 2012.
- [190] Laurent Larger, Bogdan Penkovsky, and Yuri Maistrenko. Virtual chimera states for delayed-feedback systems. *Phys. Rev. Lett.*, 111(5):054103, 2013.
- [191] Erik Andreas Martens, Shashi Thutupalli, Antoine Fourrière, and Oskar Halatschek. Chimera states in mechanical oscillator networks. *Proc. Natl Acad. Sci.*, 110(26):10563–10567, 2013.
- [192] Jerzy Wojewoda, Krzysztof Czołczynski, Yuri Maistrenko, and Tomasz Kapitaniak. The smallest chimera state for coupled pendula. *Sci. Rep.*, 6, 2016.
- [193] Laurent Larger, Bogdan Penkovsky, and Yuri Maistrenko. Laser chimeras as a paradigm for multistable patterns in complex systems. *Nat. Commun.*, 6, 2015.

- [194] Joniald Shena, Johanne Hizanidis, Vassilios Kovanis, and George P Tsironis. Turbulent chimeras in large semiconductor laser arrays. *Sci. Rep.*, 7:42116, 2017.
- [195] Emmanuelle Tognoli and JA Scott Kelso. The metastable brain. *Neuron*, 81(1):35–48, 2014.
- [196] Daniel M Abrams, Rennie Mirollo, Steven H Strogatz, and Daniel A Wiley. Solvable model for chimera states of coupled oscillators. *Phys. Rev. Lett.*, 101(8):084103, 2008.
- [197] Mark J Panaggio and Daniel M Abrams. Chimera states: coexistence of coherence and incoherence in networks of coupled oscillators. *Nonlinearity*, 28(3):R67, 2015.
- [198] David J Bergman and Mark I Stockman. Surface plasmon amplification by stimulated emission of radiation: quantum generation of coherent surface plasmons in nanosystems. *Phys. Rev. Lett.*, 90(2):027402, 2003.
- [199] Nikolay I Zheludev, SL Prosvirnin, N Papasimakis, and VA Fedotov. Lasing spaser. *Nat. Photon.*, 2(6):351–354, 2008.
- [200] Mark I Stockman. Spasers explained. *Nat. Photon.*, 2(6):327–329, 2008.
- [201] Costas M Soukoulis, Stefan Linden, and Martin Wegener. Negative refractive index at optical wavelengths. *Science*, 315(5808):47–49, 2007.
- [202] E Plum, VA Fedotov, P Kuo, DP Tsai, and NI Zheludev. Towards the lasing spaser: controlling metamaterial optical response with semiconductor quantum dots. *Opt. Express*, 17(10):8548–8551, 2009.
- [203] Shumin Xiao, Vladimir P Drachev, Alexander V Kildishev, Xingjie Ni, Uday K Chettiar, Hsiao-Kuan Yuan, and Vladimir M Shalaev. Loss-free and active optical negative-index metamaterials. *Nature*, 466(7307):735–738, 2010.
- [204] Peter Nordlander, C Oubre, E Prodan, K Li, and MI Stockman. Plasmon hybridization in nanoparticle dimers. *Nano Lett.*, 4(5):899–903, 2004.
- [205] B Willingham, DW Brandl, and P Nordlander. Plasmon hybridization in nanorod dimers. *Appl. Phys. B*, 93(1):209–216, 2008.
- [206] Frederick Reif. *Fundamentals of statistical and thermal physics*. Waveland Press, 2009.
- [207] Martin G Blaber, Matthew D Arnold, and Michael J Ford. Search for the ideal plasmonic nanoshell: the effects of surface scattering and alternatives to gold and silver. *J. Phys. Chem. C*, 113(8):3041–3045, 2009.
- [208] Gautam C Sethia and Abhijit Sen. Chimera states: the existence criteria revisited. *Phys. Rev. Lett.*, 112(14):144101, 2014.

- [209] Prashant K Jain, Susie Eustis, and Mostafa A El-Sayed. Plasmon coupling in nanorod assemblies: optical absorption, discrete dipole approximation simulation, and exciton-coupling model. *J. Phys. Chem. B*, 110(37):18243–18253, 2006.
- [210] Shih-Hui Chang and Allen Taflove. Finite-difference time-domain model of lasing action in a four-level two-electron atomic system. *Opt. Express*, 12(16):3827–3833, 2004.